INFN/AExxx, LAL-xxx, SLAC-R-xxx

Super$B$ Detector Technical Design Report

Abstract

This report describes the technical design detector for Super$B$.

Contents

1 Introduction **1**
- 1.1 The Physics Motivation . . . 1
- 1.2 The Super$B$ Project Elements . . . 1
- 1.3 The Detector Design Progress Report . . . 2

2 Accelerator Overview **5**

3 Detector Overview **7**
- 3.1 Physics Performance . . . 7
- 3.2 Challenges on Detector Design . . . 10
- 3.3 Open Issues . . . 12
- 3.4 Detector R&D . . . 12

4 Physics with SuperB **17**

5 Machine Detector Interface and Backgrounds **19**
- 5.1 Overview M.Sullivan, M. Boscolo E.Paoloni, - 1 page . . . 19
- 5.2 Backgrounds sources. M.Sullivan, M.Boscolo, E.Paoloni, - 2 pages . . . 19
- 5.3 Radiative Bhabha A.Perez - 2 pages . . . 19
- 5.4 Pairs Production C.Rimbault - 2 pages . . . 19
- 5.5 Touscheck bacgkround. M.Boscolo - 2 pages . . . 19
- 5.6 Beam gas background. M.Boscolo - 2 pages . . . 19
- 5.7 Synchrotron radiation background. M.Sullivan - 2 pages . . . 19
- 5.8 SVT background overview R.Cenci C.Stella - 2 pages . . . 20
- 5.9 DCH background overview R.Cenci D.Lindemann - 2 pages . . . 20
- 5.10 FTOF background overview L.Burmistrov - 2 pages . . . 20
- 5.11 FDIRC background overview R.Cenci A.Perez - 2 pages . . . 20
- 5.12 EMC background overview. S.Germani - 2 pages . . . 20
- 5.13 IFR background overview V.Santoro - 2 pages . . . 20
- 5.14 ETD background overview R.Cenci - 2 pages . . . 20
- 5.15 SVT radiation monitor. A.Di Ciaccio- 3 pages . . . 20
- 5.16 Quick demounting. M.Sullivan, F.Bosi, E.Paoloni - 4 pages . . . 20

6 Silicon Vertex Tracker **21**
- 6.1 Vertex Detector Overview G.Rizzo - 12 pages . . . 21
- 6.2 Backgrounds R.Cenci - 4 pages . . . 21
- 6.3 Detector Performance Studies N.Neri - 6 pages . . . 21
  - 6.3.1 Introduction *(about 1/2 page)* . . . 21
  - 6.3.2 Impact of Layer0 on detector performances *(about 2 pages)* . . . 21
  - 6.3.3 Sensitivity studies for time-dependent analyses *(about 2 pages)* . . . 21
  - 6.3.4 Vertexing and Tracking performances *(about 1 pages)* . . . 21

6.3.5 Particle Identification *(about 1/2 pages)* . . . 21
6.4 Silicon Sensors L. Bosisio - 8 pages . . . 21
6.4.1 Requirements . . . 22
6.4.1.1 Efficiency . . . 22
6.4.1.2 Resolution . . . 22
6.4.1.3 Radiation hardness . . . 22
6.4.2 Sensor design . . . 22
6.4.2.1 Technology choice . . . 24
6.4.2.2 Optimization of strip layout . . . 24
6.4.2.3 Wafer sizes and quantities . . . 24
6.4.3 Prototyping and tests . . . 24
6.5 Fanout Circuits L.Vitale - M.Prest4+4 pages . . . 24
6.5.1 Fanouts for layer0 . . . 25
6.5.1.1 Requirements . . . 25
6.5.1.2 Technology . . . 25
6.5.1.3 Design . . . 25
6.5.1.4 Prototyping and tests . . . 25
6.5.2 Fanouts for outer layers . . . 25
6.5.2.1 Requirements . . . 25
6.5.2.2 Material and production technique . . . 25
6.5.2.3 Design . . . 25
6.5.2.4 Tests and prototyping . . . 25
6.6 Electronics Readout 28 pages . . . 26
6.6.1 Readout chips V.Re - 10 . . . 26
6.6.1.1 Electronic Readout for Strip and Striplet Detectors . . . 26
6.6.1.2 Readout chips requirements . . . 27
6.6.1.3 Readout Chip Implementation . . . 29
6.6.1.4 R&D for strip readout chips . . . 30
6.6.2 Hybrid Design M.Citterio - 10 . . . 31
6.6.3 Data Transmission M.Citterio - 10 . . . 31
6.6.4 Power Supply - 2 . . . 31
6.7 Mechanical Support & Assembly S.Bettarini/F.Bosi - 14 pages . . . 31
6.7.1 I.R. Constraint . . . 31
6.7.2 Module Assembly . . . 31
6.7.3 Detector Assembly and Installation . . . 31
6.7.3.1 Half Detector Assembly . . . 31
6.7.3.2 Mount L0 on the Be-pipe and L 1-5 on the W Shielding . . . 31
6.7.3.3 Installation of Complete Assembly into the SuperB Detector . . . 31
6.7.3.4 Quick Demounting . . . 31
6.7.4 Detector Placement and Survey . . . 32
6.7.4.1 Placement accuracy . . . 32
6.7.4.2 Survey with tracks . . . 32
6.7.5 Detector Monitoring . . . 32
6.7.5.1 Position Monitoring System . . . 32
6.7.5.2 Radiation Monitoring . . . 32
6.7.6 R&D Program . . . 32
6.7.6.1 Cables . . . 32

6.7.6.2 hybrid . . . 32
6.7.6.3 Inner layer sextant . . . 32
6.7.6.4 Arch modules . . . 32
6.7.6.5 Cones and space frame . . . 32
6.7.6.6 Full-scale model of IR . . . 32
6.8 Layer0 Upgrade Options G.Rizzo/L.Ratti - 10 pages . . . 32
6.8.1 Technology options . . . 32
6.8.1.1 Hybrid pixels . . . 33
6.8.1.2 Deep N-well CMOS monolithic sensors . . . 34
6.8.1.3 Monolithic pixels in CMOS quadruple well technology . . . 35
6.8.2 R&D activity . . . 35
6.8.2.1 Front-end electronics for hybrid pixels in planar and 3D CMOS technology . . . 35
6.8.2.2 The Apsel DNW MAPS series . . . 37
6.8.2.3 The Apsel4well quadruple well monolithic sensor . . . 39
6.8.3 Radiation tolerance . . . 39
6.9 Services, Utilities and E.S. & H issues - 8 pages . . . 40
6.9.1 Service and Utilities . . . 40
6.9.2 ES&H Issue . . . 40

7 Drift Chamber - Finocchiaro, Roney 60 pages 47
7.1 Overview - Finocchiaro, Roney 12 pages . . . 47
7.1.1 Physics requirements - 3 pages . . . 47
7.1.2 Geometrical constraints - 1 page . . . 47
7.1.3 Machine background considerations - 2 pages . . . 47
7.1.4 DCH design overview - 2 pages . . . 47
7.1.5 Expected performance - 2 pages . . . 47
7.1.6 Tracking software and pattern recognition - 2 pages . . . 47
7.2 Optimization of chamber operation - Finocchiaro, Hearty, Piccolo, Roney 9 pages . 47
7.2.1 Prototype studies . . . 47
7.2.2 Gas Mixture Optimization . . . 47
7.2.2.1 Physics performance considerations . . . 47
7.2.2.2 Aging studies: fields, gas gain . . . 47
7.2.3 Cluster Counting . . . 47
7.3 Mechanical Design - Finocchiaro, Lauciani 9 pages . . . 47
7.3.1 Endplates . . . 47
7.3.2 Inner cylinder . . . 47
7.3.3 Outer Cylinder . . . 47
7.3.4 Cell structure . . . 47
7.3.5 Choice of wire and electrostatic stability . . . 47
7.3.6 Feed-through design . . . 47
7.3.7 Endplate system . . . 47
7.3.7.1 Supports for on-detector boards . . . 47
7.3.7.2 Cooling . . . 47
7.3.7.3 Shielding . . . 47
7.3.8 Stringing . . . 47

7.4 Electronics - Felici, Martin 12 pages . . . 47
7.4.1 Design Goals . . . 47
7.4.1.1 Specifications for charge measurements . . . 47
7.4.1.2 Specifications for time measurements . . . 47
7.4.2 DCH Front-end system (block diagram) . . . 47
7.4.3 On-detector electronics . . . 47
7.4.3.1 Preamplifier . . . 47
7.4.3.2 Cabling . . . 47
7.4.4 Off-detector electronics . . . 47
7.4.4.1 Triggered data path . . . 47
7.4.4.2 Non-triggered data path . . . 47
7.4.5 Optical Links . . . 48
7.4.5.1 Patch panels . . . 48
7.5 High Voltage system - Martin 1 page . . . 48
7.5.1 Main HV system . . . 48
7.5.2 Distribution boards . . . 48
7.6 Gas system - Roney 2 pages . . . 48
7.7 Calibration and monitoring - Roney 3 pages . . . 48
7.7.0.1 Slow control systems . . . 48
7.7.0.2 Calibration . . . 48
7.7.0.3 Gas monitoring system . . . 48
7.7.0.4 On-line monitor . . . 48
7.8 Integration - Hearty, Lauciani 6 pages . . . 48
7.8.1 Overall geometry and mechanical support . . . 48
7.8.2 Cable supports and routing . . . 48
7.8.3 Access . . . 48
7.8.4 Gas system . . . 48
7.8.5 Off-detector electronics crates . . . 48
7.8.6 High voltage crates . . . 48
7.8.7 Installation and alignment . . . 48
7.9 R&D Program - Finocchiaro, Piccolo 6 pages . . . 48
7.9.1 Results . . . 48
7.9.2 Plans . . . 48

8 Particle Identification 51
8.1 Summary of Physics Requirements and Detector Performance goals 3-4 pages . . . 51
8.1.1 Physics requirements Cincinnati, Maryland . . . 51
8.1.2 Detector concept . . . 51
8.1.3 Charged Particle Identification . . . 52
8.2 Particle Identification Overview 2-3 pages . . . 52
8.2.1 Experience of BaBar DIRC . . . 52
8.2.2 Barrel PID: Focusing DIRC (FDIRC) . . . 53
8.3 Projected Performance of FDIRC 2-3 pages . . . 56
8.3.1 Reconstruction Arnaud, Roberts . . . 56
8.3.2 MC Simulation . . . 56
8.3.3 Effect of Background on performance Cenci, Vavra, Kravchenko . . . 57

8.4 The Barrel FDIRC Detector Overview 5-10 pages . . . 57
8.4.1 Impact on other systems Benettoni, Simi, Vavra . . . 57
8.4.2 Photodetectors . . . 57
8.4.3 Laser calibration system . . . 65
8.4.4 FDIRC Mechanical Design 5 pages . . . 66
8.4.5 Mechanical support . . . 66
8.4.6 Electronics readout, High and Low voltage . . . 73
8.4.7 Integration issues 2 pages . . . 76
8.4.8 DAQ and computing 1 page . . . 77
8.4.9 FDIRC R&D Results until now 2-3 pages . . . 77
8.4.10 Ongoing FDIRC R&D 1-2 pages . . . 77
8.4.11 System Responsibilities and Management 1-2 pages . . . 78
8.4.12 Cost, Schedule and Funding Profile 1-2 pages . . . 78

9 Electromagnetic Calorimeter 83
9.1 Overview . . . 83
9.1.1 Background and radiation issues . . . 83
9.1.2 Simulation tools . . . 85
9.1.2.1 Fastsim . . . 85
9.1.2.2 Full sim . . . 85
9.2 Barrel Calorimeter . . . 85
9.2.1 Requirements Relevant to the Super$B$ Environment . . . 86
9.2.1.1 Crystal Aging at *BABAR* . . . 86
9.2.1.2 Backgrounds . . . 86
9.2.2 Description of *BABAR* Barrel Calorimeter . . . 86
9.2.2.1 Mechanical design . . . 86
9.2.2.2 Readout . . . 89
9.2.2.3 Calibration . . . 89
9.2.3 Performance of *BABAR* barrel . . . 89
9.2.3.1 Energy and position resolution . . . 89
9.2.3.2 Gamma-gamma mass resolution . . . 89
9.2.3.3 Radiation Damage Effects on Resolution . . . 89
9.2.3.4 Expected Changes in Performance at Super$B$ . . . 89
9.2.4 Electronics changes . . . 89
9.2.4.1 Rationale for changes . . . 89
9.2.4.2 Premp design . . . 89
9.2.4.3 Shaping and digitization . . . 89
9.2.4.4 Cabling . . . 89
9.2.5 SLAC De-installation, Transport and Local Storage . . . 89
9.2.6 Electronics refurbishment . . . 89
9.2.7 Calibration systems . . . 89
9.2.8 Re-installation at Tor Vergata . . . 89
9.3 Forward Calorimeter . . . 89
9.3.1 Requirements[RF] . . . 90
9.3.2 LYSO Crystals[RZ] . . . 90
9.3.3 Introduction . . . 90

9.3.4 Optical and Scintillation Properties . . . 91
9.3.4.1 Transmittance and Emission . . . 91
9.3.4.2 Decay time and Light Output . . . 96
9.3.5 Light Collection and Response Uniformity . . . 97
9.3.6 Radiation Hardness . . . 100
9.3.7 Specifications, Production and Testing . . . 103
9.3.8 Readout and Electronics[VB] . . . 106
9.3.8.1 APD Readout[DH] . . . 106
9.3.8.2 Electronics Block diagram . . . 107
9.3.8.3 Preamplifier . . . 107
9.3.8.4 Shaper . . . 107
9.3.8.5 Digitization . . . 107
9.3.8.6 Requirements on mechanics . . . 107
9.3.9 Calibrations[DH] . . . 107
9.3.9.1 Initial calibration with source . . . 107
9.3.9.2 Electronics calibration . . . 108
9.3.9.3 Temperature monitoring and correction . . . 108
9.3.10 Mechanical Design[CG] . . . 110
9.3.10.1 Introduction and parameters . . . 110
9.3.10.2 General contraints and requirements . . . 110
9.3.10.3 Cooling and Calibration requirements . . . 111
9.3.10.4 Crystal sub-unit design . . . 112
9.3.10.5 Module design . . . 112
9.3.10.6 Alveolar module structure finite element analysis . . . 118
9.3.10.7 Support shell structure design . . . 118
9.3.10.8 Global structure finite element analysis . . . 120
9.3.11 Performance in simulations[SG] . . . 120
9.3.11.1 Resolution studies . . . 120
9.3.11.2 Background studies . . . 120
9.3.12 Tests on Beam[CC] . . . 120
9.3.12.1 Description of apparatus . . . 120
9.3.12.2 Description of the beams . . . 121
9.3.12.3 Description of data and calibration . . . 123
9.3.12.4 Electronics noise measurements . . . 124
9.3.12.5 Temperature corrections . . . 126
9.3.12.6 Algorithms and results . . . 126
9.3.13 Alternatives . . . 126
9.3.13.1 Pure CsI . . . 126
9.3.13.2 BGO . . . 126
9.3.13.3 Hybrid Alternative . . . 127
9.3.13.4 Comparison with baseline . . . 127
9.4 Backward Calorimeter . . . 128
9.4.1 Requirements . . . 129
9.4.1.1 Energy and angular resolution . . . 129
9.4.1.2 Background rates . . . 130
9.4.1.3 Radiation hardness . . . 130
9.4.1.4 Solid angle, transition to barrel . . . 130

9.4.2 Mechanical design . . . 131
9.4.2.1 Calorimeter construction . . . 132
9.4.2.2 Support and services . . . 132
9.4.3 SiPM/MPPC readout . . . 132
9.4.4 Electronics . . . 133
9.4.5 Calibration . . . 133
9.4.6 Backward simulation . . . 134
9.4.7 Impact on physics results . . . 135
9.4.8 Impact on particle identification . . . 138
9.4.9 Discussion of task force conclusions . . . 138
9.5 Trigger . . . 141
9.5.1 Calorimeter readout trigger . . . 141
9.5.1.1 Normal mode . . . 141
9.5.1.2 Calibration mode . . . 141
9.5.2 Calorimeter trigger primitives . . . 141
9.6 Detector protection . . . 141
9.6.1 Thermal shock . . . 141
9.6.2 Mechanical shock, including earthquakes . . . 141
9.6.3 Fluid spills . . . 141
9.6.4 Electrical surges, outages . . . 141
9.6.5 Radiation damage . . . 141
9.7 Cost & Schedule . . . 142
9.7.1 WBS structure . . . 142
9.7.2 Gantt chart . . . 142
9.7.3 Basis of estimates . . . 142
9.7.4 Cost and schedule risks . . . 142

10 Instrumented Flux Return **145**
10.1 Performance Optimization . . . 146
10.1.1 Identification Technique . . . 146
10.1.2 Baseline Design Requirements . . . 147
10.1.3 Design Optimization and Performance Studies . . . 147
10.2 R&D Work . . . 148
10.2.1 R&D Tests and Results . . . 149
10.2.2 Prototype . . . 150
10.3 Baseline Detector Design . . . 151
10.3.1 Flux Return . . . 151

11 Magnet and Flux Return **155**

12 Trigger, DAQ and Online **157**
12.1 Overview of the Architecture . . . 157
12.1.1 Trigger Strategy . . . 158
12.1.2 Trigger Rates and Event Size Estimation . . . 159
12.1.3 Dead Time and Buffer Queue Depth Considerations . . . 160
12.1.4 Fast Control and Timing System . . . 161
12.1.5 Readout Module . . . 163
12.1.6 Experiment Control System . . . 163

12.1.7 Level 1 Hardware Trigger . . . 165
12.2 Online System . . . 166
12.2.1 ROM Readout and Event Building . . . 166
12.2.2 High Level Trigger Farm . . . 167
12.2.3 Data Logging . . . 167
12.2.4 Event Data Quality Monitoring and Display . . . 167
12.2.5 Run Control System . . . 168
12.2.6 Detector Control System . . . 168
12.2.7 Other Components . . . 168
12.2.8 Software Infrastructure . . . 169
12.3 Front-End Electronics . . . 169
12.4 R&D . . . 169
12.5 Conclusions . . . 170
12.6 Organizational Structure of Electronics, Trigger, DAQ and Online . . . 171

13 Electronics **175**
13.1 Electronics overview . . . 175
13.2 Common components . . . 175
13.2.1 Clock, Control and Data Links . . . 175
13.2.2 FCTS Links . . . 177
13.2.3 Data Links . . . 177
13.2.4 Common Front-End Electronics . . . 177
13.2.5 Power supplies (?) . . . 178
13.2.6 Cable Plant (?) . . . 178
13.3 Subsystem-specific Electronics . . . 178
13.3.1 SVT Electronics . . . 178
13.3.2 DCH Electronics . . . 179
13.3.3 PID Electronics . . . 180
13.3.4 EMC Electronics . . . 182
13.3.5 IFR Electronics . . . 183
13.3.6 Level-1 Trigger Electronics . . . 184

14 Software and Computing **185**
14.1 The Super$B$ baseline model . . . 186
14.1.1 The requirements . . . 187
14.1.2 Super$B$ offline computing development . . . 188
14.2 Computing tools and services for the Detector and Physics TDR studies . . . 188
14.2.1 Fast simulation . . . 188
14.2.2 Bruno: the Super$B$full simulation tool . . . 193
14.2.3 The distributed production environment . . . 195
14.2.4 The software development and collaborative tools . . . 199
14.2.5 Code packaging and distribution . . . 200

15 Environmental Safety and Health **203**

16 Facilities, Mechanical Integration and Assembly **205**
16.1 Introduction . . . 205
16.1.1 Magnet and Instrumented Flux Return . . . 206

16.2 Component Extraction 207
16.3 Component Transport 208
16.4 Detector Assembly 209

17 Project Management **211**

18 Cost and Schedule **213**
18.1 Detector Costs 214
18.2 Basis of Estimate 218
18.3 Schedule 221

9 Electromagnetic Calorimeter

9.1 Overview

Calorimetry at Super$B$ is achieved with three major components: A CsI(Tl) "barrel" calorimeter covering the central region, a LYSO(Ce) "forward" calorimeter covering the small angle region in the direction of the high energy beam, and a lead-scintillator "backward" calorimeter covering the small angle region in the direction of the low energy beam. Table 9.1 shows the solid angle coverage for each of the three parts of the SuperB EMC. The superB electromagnetic calorimeter (EMC) will play an essential role in the study of the flavor physics especially in the sector in which B meson decays involve neutral particles. The calorimeter provides energy and direction measurement of photons and electrons, reconstruction of neutral hadrons such as π^0's and discrimination between electrons and charged hadrons. Many channels containing missing energy due to the presence of neutrinos will rely on information from the EMC to discriminate against backgrounds.

The SuperB EMC reuses the barrel part of the BaBar EMC detector consisting of 5760 CsI(Tl) crystals as shown in Fig. **??**. However the *BABAR* forward calorimeter will need to be replaced, due to the higher radiation and higher rates at SuperB compared with PEP-II. The forward endcap will be replaced by a new scintillating crystal calorimeter designed to work well in this new environment. Compared with the BaBar calorimeter where good energy and position resolution are required, the same criteria apply for SuperB. After an intensive R&D program the baseline option for the SuperB forward calorimeter is to use the faster and more radiation resistant LYSO crystals. As will be discussed below, this is the clear favorite in terms of performance and radiation hardness over the alternatives we have considered. The faster response time and shorter Moliére radius serve together to address the higher event and background rates. LYSO is a fast scintillator largely used in medical applications with crystals of small size. The R&D was concentrated on the optimization of performance for large crystals (2cm x 2 cm x 20 cm) with good light yield uniformity and optimized Ce doping in order to have the best possible light output. Thanks to this effort, more than one producer is able to grow LYSO crystals of good quality that can be used in high energy physics applications. Table **??** shows the comparison between LYSO and other materials used in electromagnetic calorimeters. The largest disadvantage of LYSO is cost, and we have studied lower cost alternatives as described below.

Finally, a lead-scintillator-sandwich backward endcap calorimeter improves the hermeticity of the detector. The main purpose of this component is to detect energy in the bacward endcap region, as a veto of with extra "extra" energy. This is particularly important for studying channels with neutrinos in the final state. Because of the fast time response, the backward EMC may also have a role in particle identification by providing time-of-flight for the relatively slow backward-going charged particles.

9.1.1 Background and radiation issues

One of the major concerns for the electromagnetic calorimeter is its capability to sustain the radiation dose, dose which is larger than in previous experiments due to the increased luminosity. The dominant contribution to radiation in SuperB is in fact expected to come from radiative bhabha events, that emit a large number of low energy photons at an extremely high rate. This photon rate can impact the performances

Table 9.1: Solid angle coverage of the electromagnetic calorimeters. Values are obtained assuming the barrel calorimeter is in the same location with respect to the collision point as for *BABAR*. The CM numbers are for massless particles and nominal 4 on 7 GeV beam energies. The barrel Super*B* row includes one additional ring of crystals over *BABAR*.

Calorimeter	$\cos\theta$ (lab)		$\cos\theta$ (CM)		Ω (CM)(%)
	minimum	maximum	minimum	maximum	
Backward	-0.974	-0.869	-0.985	-0.922	3.1
Barrel (*BABAR*)	-0.786	0.893	-0.870	0.824	84.7
Barrel (Super*B*)	-0.805	0.893	-0.882	0.824	85.2
Forward	0.896	0.965	0.829	0.941	5.6

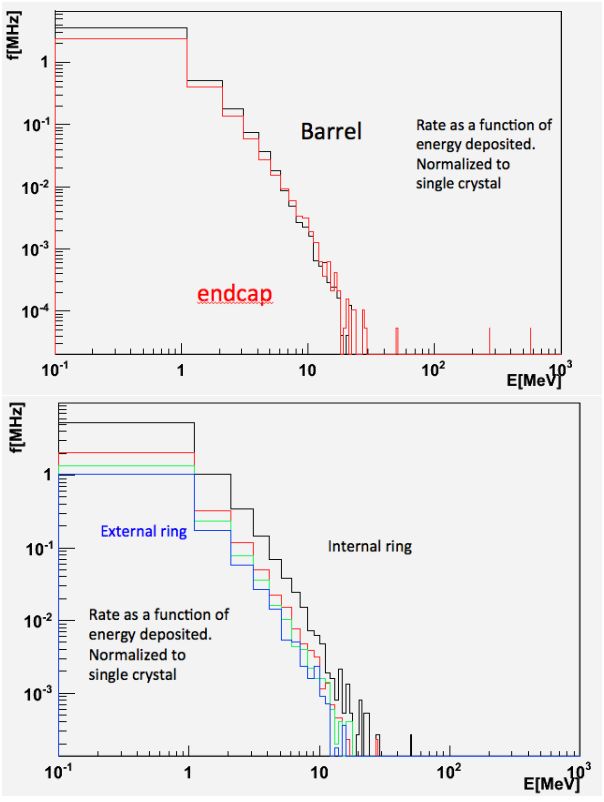

Figure 9.1: Machine Background rates per crystal as a function of deposited energy.

of the detector because of two effects: the radiation can reduce the transmittance of the crystals and therefore alter as a function of time the calibration of the detector; the large number of photons can pile-up with the other effects thus introducing a degradation in energy resolution.

To estimate the impact of these effect a full simulation has been setup as described in Sec.**WHICH SECTION?**. The simulation outputs the energy deposited by radiative Bhabha events in the individual crystals at each beam crossing. i.e. every 2.1ns. This can be converted in terms of rate of photons of a given energy impacting each crystal. The result is shown in Fig. 9.1, both (left) averaging over the whole Barrel and the whole FWD and (right) averaging over the rings of the FWD which have the same number of crystals per ring. The result shows that there is no significant difference in the irradiation between the Barrel and the Endcap. This can be understood because the dimension of the crystals is significantly different: due the different density and consequently molier radius, the transverse dimensions of LYSO or BGO crystals are two times smaller than the CsI crystals (both doped and not) and the overall volume of a LYSO or BGO crystal is 6.7 times smaller (120cm^3 vs 800cm^3) than the CsI ones. Since the rates of signals from the machine background scales linearly with volume, the most forward crystals of the Barrel will suffer a background more than six times larger than the more central crystals of the FWD calorimeter, albeit contiguous.

On average therefore each crystal (both of Barrel or Endcap) will see 1MHz of photons between 1 and 5 MeV and 10 KHz of photons between 5-10 MeV. A plausible linear extrapolation in log-log scale would lead to 100Hz between 10-50 MeV and 1Hz between 50-100 MeV.

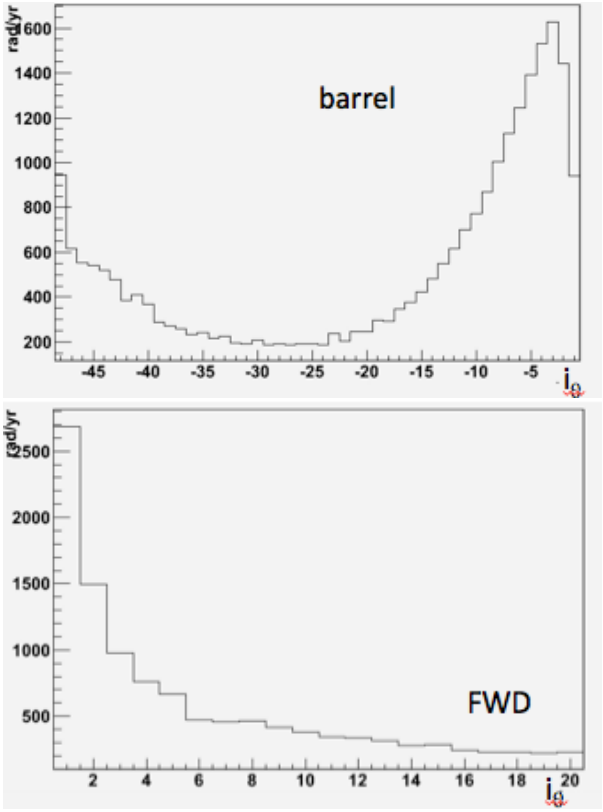

Figure 9.3: Integrated dose as a function of i_θ for the Barrel (Left) and FWD (Right) EMC.

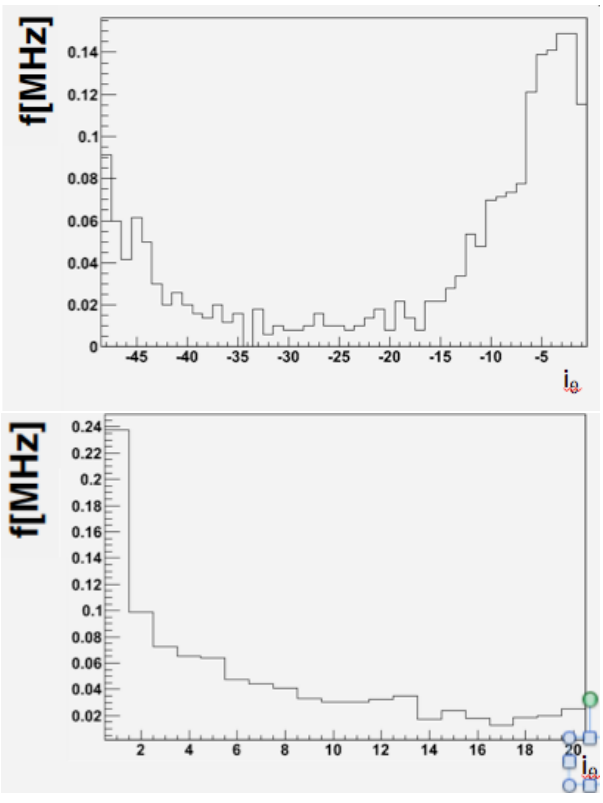

Figure 9.2: Integrated rates for $E > 5$MeV as a function of $i_\theta$for the Barrel (Left) and FWD (Right) EMC.

The ring-by-ring details are shown in Fig. 9.2, where the integrated rate of deposits larger than 5MeV are estimated as a function of an index, i_θ which is $i_\theta < -49$ for the backward calorimeter, $-49 =< i_\theta < 0$ for the barrel ($i_\theta = -1$ corresponding to the most forward ring), and $i_\theta > 0$ for the FWD EMC ($i_\theta = 1$ corresponding to the innermost ring) . It can be noted that the forward region of the barrel ($i_\theta > -10$) is more irradiated than the FWD calorimeter, a part from the innermost ring which is a factor two worse than any other ring.

From the radiation hardness point of view, the dose to which the crystals are sensitive is defined as the total energy deposited in a crystal divided by its mass. The dose expected per year (conventionally considered $10^7 s$ long) and per crystal is shown in Fig 9.3 separately for the Barrel and the FWD. Conservatively, assuming a maximum of 10 years of operations, crystals need to be radiation resistent up to at least 30krad. Also the impact on resolution of a $\sim$ 1rad/hour dose rate needs to be considered.

9.1.2 Simulation tools

9.1.2.1 Fastsim

9.1.2.2 Full sim

9.2 Barrel Calorimeter

We propose to re-use the barrel portion of the *BABAR* EMC, retaining the fundamental mechanical structures and the 5760 CsI(Tl) crystals and associated pairs of photodiodes mounted on each crystal, along with some modifications required for optimal performance at Super$B$.

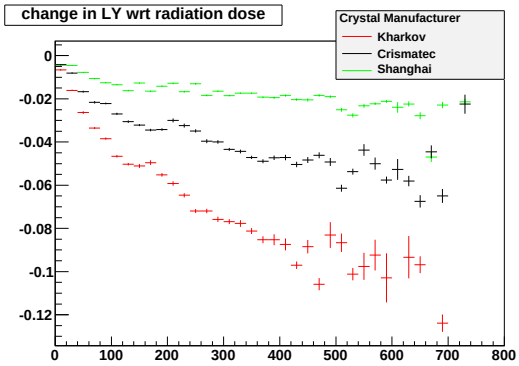

(a) Barrel Backward

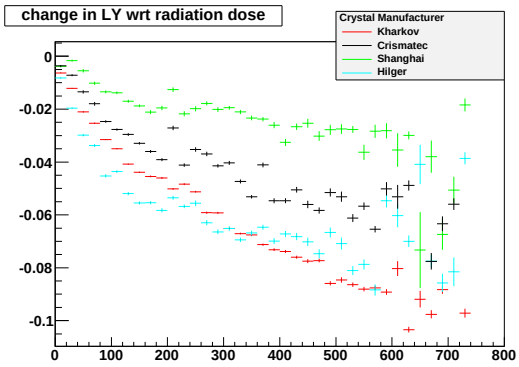

(b) Barrel Forward

Figure 9.4: Barrel crystal light yield decreases plotted with respect to absorbed radiation dose, with the different crystal manufacturers indicated.

9.2.1 Requirements Relevant to the SuperB Environment

9.2.1.1 Crystal Aging at BABAR

Over the span of Babar's running, the EMC barrel crystals have been damaged to a certain extent by high levels of radiation, which was monitored by 116 radFETs distributed throughout the subdetector. The most common form of damage [**?**] comes from the development of absorption bands which reduce an affected crystal's light yield. Although crystals in the EMC endcap experienced higher levels of radiation than those in the barrel, all EMC crystals from the furthest backward to those more forward integrated non-negligible doses. The resulting changes in crystal light yields were monitored and corrected for during Babar operation using calibrations performed at either end of the dynamic range of the detector: a low-energy calibration using a 6.13 MeV radioactive photon source, which is discussed below in Sec. **??**, and a high-energy calibration with Bhabha events.

The change in light yield for barrel crystals as a function of absorbed radiation dose, based on the low-energy calibration data, is shown categorized by crystal manufacturer in Figure 9.4. Though care was initially taken to produce uniformity between crystals before they were integrated into the detector, there have been varying degrees of degradation in performance as time has progressed. Depending on the manufacturer, the total decrease in light yield can be up to $\sim 10\%$. Clearly, in the Super-B environment, the eventual loss in light yield for the worst-performing barrel crystals is likely to be substantial.

9.2.1.2 Backgrounds

In addition to crystal aging, background can degrade energy resolution due to electronic signal pile-up. The dominated source is expected to be photons and neutrons from radiative Bhabha events interacting with the detector material. This effect is negligible in *BABAR*. But in Super$B$, it could be substantial, especially in the low energy range.

The pile-up effect is a function of signal pulse shape. Since Super$B$ is reusing *BABAR*'s barrel, the long decay time of CsI(Tl) crystal cannot be changed. Nonetheless, readout and electronics can be optimized to minimize the the impact of the pile-up effect. To ensure similar physics sensitivity as *BABAR*, the background pile-up should have a negligible effect in energy resolution of high energy photons (*how high?*) and contribute to no more than $x\%$ to energy resolution of photons at 100 MeV.

9.2.2 Description of BABAR Barrel Calorimeter

9.2.2.1 Mechanical design

The Babar barrel EMC consists of a cylindrical barrel with full azimuthal coverage, extending in

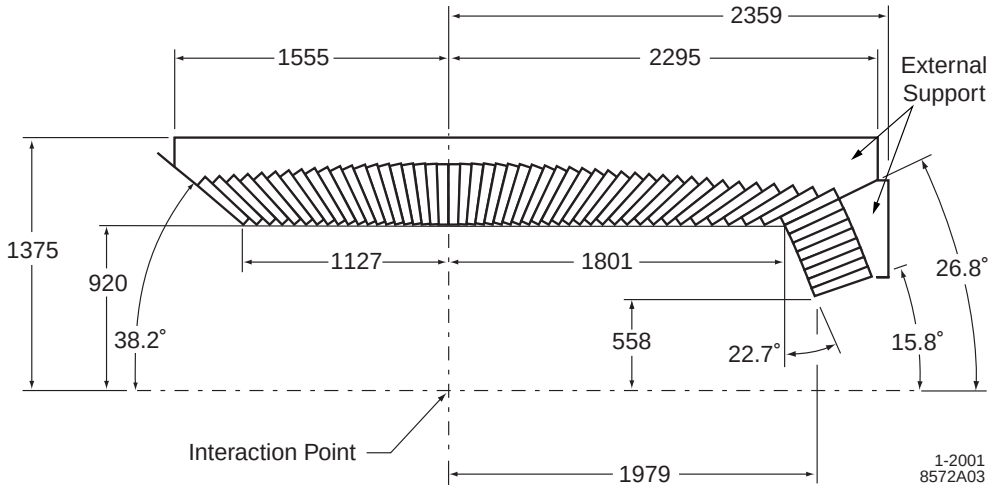

Figure 9.5: Longitudinal EMC cross-section (only the top half is shown) indicating the arrangement of the 48 barrel and 8 endcap crystal rings. The detector is axially symmetric around the z-axis. All dimensions are in mm.

polar angle from 26.8° to 141.8°. A longitudinal cross-section, including the forward endcap, is shown in Figure 9.5. The barrel EMC contains 5,760 crystals arranged in 48 separate azimuthal rings, with 120 identically dimensioned crystals in each ring. Each crystal has a tapered trapezoidal cross section, with length increasing from 29.6 cm furthest backward to 32.4 cm furthest forward in order to minimize the effects of shower leakage from increasingly higher energy particles. To minimize the probability of preshowers, the crystals are completely supported at the outer radius, with only a thin gas seal at the front. The amount of material in front of the crystal faces is $0.3 - 0.6X_0$.

Figure 9.6 is a not-to-scale schematic of a single crystal, showing the layered crystal wrappings, silicon photodiodes, diode carrier plate, preamplifier and the aluminum housing enclosing the items at the crystal rear face. The existing photon detector consists of two $2 \times 1\,\mathrm{cm}^2$ silicon PIN diodes glued to a transparent 1.2 mm-thick polysterene substrate that, in turn, is glued to the center of the rear face of the crystal by an optical epoxy to maximize light transmission. The surrounding area of the crystal face is covered by a plastic plate coated with white reflective paint. The plate has two 3 mm-diameter penetrations for the fibers of the light pulser monitoring system.

The signal from each of the diodes is transmitted to the preamplifier through a cable terminated in a connector which allows straightforward decoupling of the preamplifier from the photodiodes. The entire assembly at the crystal's rear face is enclosed in an aluminum housing which is electrically coupled to the aluminum foil wrapped around the crystal, as well as thermally coupled to the support frame to dissipate the heat load from the preamplifiers.

The barrel crystals are inserted into modules that are supported individually from an external cylindrical support structure. At Babar, the barrel support cylinder carries the load of the barrel modules plus the forward endcap to the magnet iron through four flexible supports, which decouple and dampen any acceleration induced by movements of the magnet iron during a potential earthquake.

The crystal modules are built from tapered, trapezoidal compartments made from carbon-fiber-epoxy composite (CFC) with 300 μm-thick walls. Each compartment loosely holds a single wrapped and instrumented crystal, assuring that the forces on the crystal surfaces never ex-

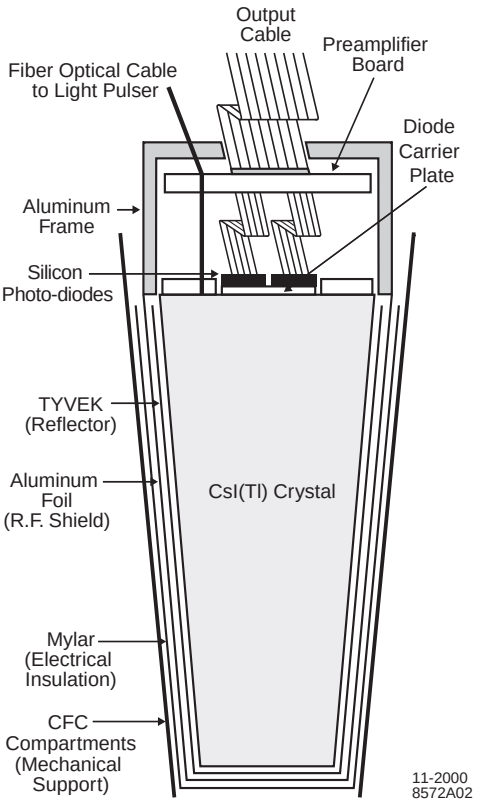

Figure 9.6: A schematic (not to scale) of a wrapped barrel crystal and the front-end readout package mounted on the rear face. Also indicated is the tapered, trapezoidal CFC compartment, which is open at the front.

ceed its own weight. Each module is surrounded by an additional layer of 300 μm CFC to provide additional strength. The modules are bonded to an aluminum strong-back that is mounted on the external support structure. Figure 9.7 shows some details of a module and its mounting to the support cylinder. This scheme minimizes inter-crystal materials while exerting minimal force on the crystal surfaces, preventing geometric deformations and surface degradation that could compromise performance.

The barrel is divided into 280 separate modules, each holding 21 crystals (7×3 in $\theta \times \phi$), except for the furthest backward modules which are only 6×3. After insertion of the crystals, the aluminum readout frames, which also stiffen the module, were attached with thermally-conducting epoxy to each of the CFC compartments. The entire $\sim$ 100 kg module is then bolted and again thermally epoxied to an aluminum strong-back, which is shown in Figure 9.7. The strong-back contains alignment features as well as channels that couple to the cooling system. Each module was installed into the 2.5 cm-thick, 4 m-long aluminum support cylinder, and subsequently aligned. On each of the thick annular end-flanges, the support cylinder contains access ports for digitizing electronics crates with associated cooling channels, as well as mounting features and alignment dowels for the forward endcap. Figure 9.7 shows details of an electronics mini-crate situated within the support cylinder.

The primary heat sources internal to the calorimeter are the preamplifiers (2×50) mw/crystal and the digitizing electronics (3 kw per end-flange). In the barrel, the preamplifier heat is removed by conduction to the module strong backs which are directly cooled by Fluorinert (polychlorotrifluoro-ethylene). The digitizing electronics are housed in 80 mini-crates, each in contact with the end-flanges of the cylindrical support structure. These crates are indirectly cooled by chilled water pumped through channels milled into the end-flanges close to the inner and outer radii.

The entire barrel is surrounded by a double Faraday shield composed of two 1 mm-thick aluminum sheets so that the diodes and preamplifiers are further shielded from external noise. This cage also serves as the environmental barrier, allowing the slightly hygroscopic crystals to reside in a dry, temperature-controlled nitrogen atmosphere.

Similar to how it has been maintained throughout its existence, the EMC barrel is currently stored at a constant, accurately monitored temperature, During Babar data-taking, of particular concern were the stability of the photodiode leakage current, which rises exponentially with temperature, and crystal light yield, which is weakly temperature dependent. Currently, the most important issue is that the

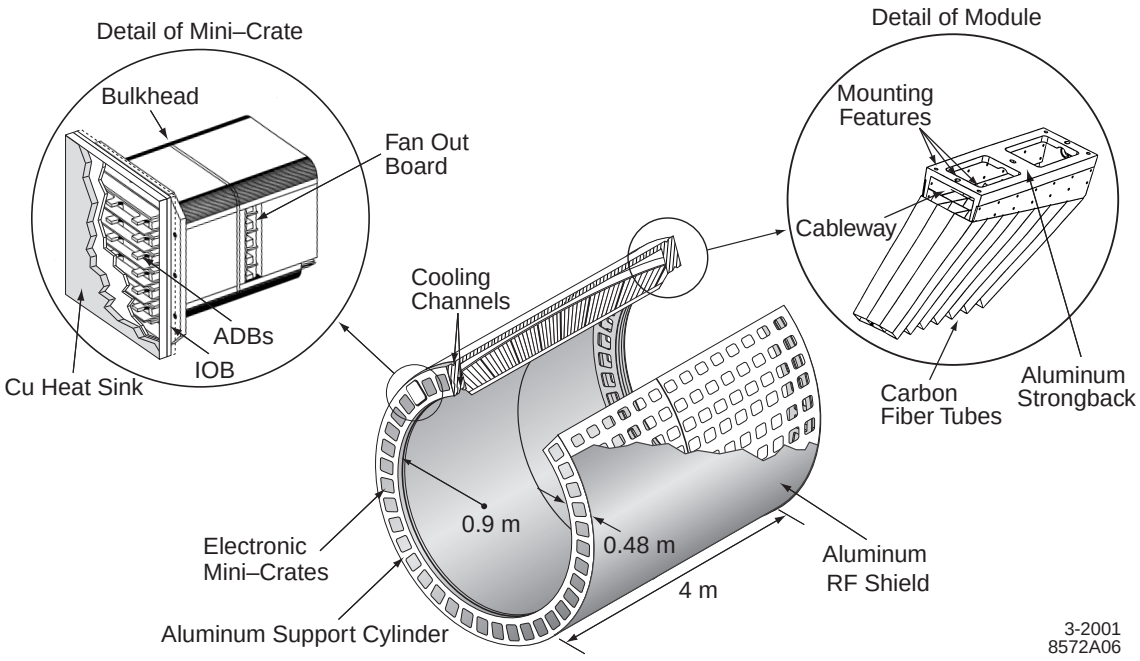

Figure 9.7: The EMC barrel support structure, with details on the modules and electronics crates (not to scale).

large number of diode-crystal epoxy joints experience as little stress as possible due to differential thermal expansion.

9.2.2.2 Readout

9.2.2.3 Calibration

9.2.3 Performance of BABAR barrel

9.2.3.1 Energy and position resolution

9.2.3.2 Gamma-gamma mass resolution

9.2.3.3 Radiation Damage Effects on Resolution

9.2.3.4 Expected Changes in Performance at SuperB

9.2.4 Electronics changes

9.2.4.1 Rationale for changes

9.2.4.2 Premp design

9.2.4.3 Shaping and digitization

Synopsis, main discussion in electronics chapter(?)

9.2.4.4 Cabling

changes?

9.2.5 SLAC De-installation, Transport and Local Storage

9.2.6 Electronics refurbishment

Repair crystals with 0/1 working channels
Preamp replacement
ADC board replacement

9.2.7 Calibration systems

Brief system description
Replace DT neutron generator
New plumbing from generator to detector
Repair and reconstitute light pulser system

9.2.8 Re-installation at Tor Vergata

9.3 Forward Calorimeter

The Forward Calorimeter is designed to extend the coverage of the electromagnetic calorimeter to low angles, as detailed in Tab. 9.1. To

be effective its performances need therefore be comparable with the Barrel Calorimeter. Thus, the design considers a calorimeter made of homogeneous crystals and read-out by compact photodetectors capable of operating in magnetic field.

As detailed in this section, the best option to fulfill the requirements described in Sec. 9.3.1 is to use crystals made of LYSO readout by Avalance Photo-Diodes (APD). In Sec. 9.3.13 we will nonetheless report the results of the investigations on other types of crystals, in case budget constraints will not allow the baseline option.

9.3.1 Requirements[RF]

Taking as benchmark the BaBar detector, the relative energy resolution need be at most 4.3% at 100 MeV and 2.7% at 1 GeV. Also, in order to assure appropriate resolution on the π^0 invariant mass and to allow the $\pi^0 \to \gamma\gamma$ reconstruction up to sufficiently high energies, a segmentation at least comparable with the BaBar one is needed. Since the transverse crystal size is dictated by the Molier radius of the material, only crystals with a Molier radius at most as large as the CsI(Tl) can be considered. Finally hermeticity is also important, so the requirement on mechanics is that the fraction of particles originating from the interaction point passing through the cracks of the

As already described for the Barrel Calorimeter, the most stringent constraints come from the presence of large background due to the extremely high luminosity. In particular, as described in Sec. 9.1.1, the large rate of low energy photons can create radiation damage on the crystal themselves, thus reducing the light yield, and induce a degradation of the energy resolution due to pile-up.

As shown in Fig. 9.3, the expected dose integrated in a year ranges from $\sim$ 200 rad for the outermost rings to $\sim$ 2500 rad for the innermost ones. Consequently, the dose rate the crystals need to tolerate ranges from $\sim$ 0.1 rad/s to $\sim$ 1.0 rad/s, respectively.

In order to estimate the effect of the pile-up on the energy resolution, the study described in Sec. 9.2.1.2 has been extended to the Forward Calorimeter. Contrarily to the case of the Barrel where only one crystal type was considered, several possible crystals were considered for the Forward. The considered options differ, for the purposes of this study only by the decay time of the signal (τ_{dec}). For a given crystal, the additional handles are the time constants of the electronics, in our case the shaping time (T_{shape}) and the time constant of the integration circuit (T_{int}). Tab. 9.2 shows the expected contribution from pile-up to the energy resolution at 100 MeV and 1 GeV. The constraint on the electronic design is therefore that the contribution to the energy resolution needs to be significantly smaller than the design resolutions of 4.3% and 2.7% respectively.

9.3.2 LYSO Crystals[RZ]

In the last two decades, cerium doped lutetium oxyorthosilicate (Lu_2SiO_5 or LSO) [1] and cerium doped lutetium yttrium oxyorthosilicate ($Lu_{2(1-x)}Y_{2x}SiO_5$ or LYSO) [2] have been developed for the medical industry with mass production capabilities established. This section addresses the issues of crystal properties, specifications, production and testing.

9.3.3 Introduction

Table 9.3 [3] lists basic properties of heavy crystals: NaI(Tl), CsI(Tl), pure CsI, bismuth gemanade ($Bi_4Ge_3O_{12}$ or BGO), lead tungstate ($PbWO_4$ or PWO) and LSO/LYSO. All have either been used in, or are actively being pursued for, high energy and nuclear physics experiments, which are also listed in the table. The experiment names in bold refer to future crystal calorimeters. NaI(Tl), CsI(Tl), BGO, LSO and LYSO crystals are also widely used in the

model	τ_{dec} (ns)	T_{shape} (ns)	T_{int} (ns)	outermost		innermost	
				100 MeV	1 GeV	100 MeV	1 GeV
LYSO	50	50	??	??	??	??	??
BGO (short)	300	100	??	??	??	??	??
BGO (long)	300	300	??	??	??	??	??
CsI(Tl) (BaBar)	1300	700	??	??	??	??	??
CsI(Tl) (short)	1300	300	??	??	??	??	??

Table 9.2: Contribution to the resolution (in %) induced by machine background on clusters for possible values of τ_{dec}, T_{shape}, and T_{int}. The first quote corresponds to an energy of 100 MeV, the second one of 1 GeV. The extreme cases of photons impinging on the outermost or innermost rings of the Forward Calorimeter were considered.

medical industry. Mass production capabilities exist for all these crystals.

Because of their high stopping power, high light yield, fast decay time, small temperature coefficient and excellent radiation hardness, LSO and LYSO crystals have attracted a broad interest in the high energy physics (HEP) community [4, 5, 6, 7], and are chosen for the baseline material for the SuperB forward calorimeter. LSO and LYSO crystals from following vendors were tested during the R&D phase of the project: CTI Molecular Imaging (CTI), Crystal Photonics, Inc. (CPI), Saint-Gobain (SG), Sichuan Institute of Piezoelectric and Acousto-optic Technology (SIPAT) and Shanghai Institute of Ceramics (SIC).

9.3.4 Optical and Scintillation Properties

9.3.4.1 Transmittance and Emission

LYSO crystals of 20 cm (18 X_0) long are routinely produced in industry. They have good transmittance spectra. The left plot of Figure 9.8 shows longitudinal (green) and transverse (red) transmittance spectra measured for a rectangular LYSO sample with a dimension of $2.5 \times 2.5 \times 20$ cm (18 X_0). Significant red shift is observed in the absorption edge of the longitudinal transmittance as compared to the transverse transmittance, which is caused by internal absorption. The black line at the top is a fit to the theoretical limit of transmittance calculated by using refraction index assuming multiple bounces between two end surfaces and no internal absorption [8]. It overlaps with the transverse transmittance spectrum at wavelengths longer than 420 nm, indicating excellent optical quality of the crystal. Also shown in this plot is the photo-luminescence spectrum (blue) [9]. The fact that a part of the emission spectrum is at the wavelengths shorter than the absorption edge indicates that this part of the scintillation light is absorbed internally in the crystal bulk, usually referred to as self-absorption effect. There is no such self-absorption effect in other scintillation crystals commonly used for HEP calorimeters, such as BGO, CsI(Tl) and PWO [3]. While this self-absorption has little consequence to 6 mm long pixels used in medical instruments, it would affect light response uniformity for 20 cm long crystals used to construct the SuperB calorimeter. This effect will be discussed in section 9.3.5.

Table 9.3: Properties of Heavy Crystal with Mass Production Capability

Crystal	NaI(Tl)	CsI(Tl)	CsI	BGO	$PbWO_4$	LSO/LYSO(Ce)
Density (g/cm^3)	3.67	4.51	4.51	7.13	8.3	7.40
Melting Point (°CC)	651	621	621	1050	1123	2050
Radiation Length (cm)	2.59	1.86	1.86	1.12	0.89	1.14
Molière Radius (cm)	4.13	3.57	3.57	2.23	2.00	2.07
Interaction Length (cm)	42.9	39.3	39.3	22.7	20.7	20.9
Refractive Index[a]	1.85	1.79	1.95	2.15	2.20	1.82
Hygroscopicity	Yes	Slight	Slight	No	No	No
Luminescence[b] (nm)	410	560	420	480	425	420
(at Peak)			310		420	
Decay Time[b] (ns)	245	1220	30	300	30	40
			6		10	
Light Yield[b,c]	100	165	3.6	21	0.30	85
			1.1		0.077	
d(LY)/dT[b,d] (%/°CC)	-0.2	0.4	-1.4	-0.9	-2.5	-0.2

Experiment	Crystal	CLEO	kTeV	L3	CMS	**Mu2e**
	Ball	*BaBar*		BELLE	ALICE	**SuperB**
		BELLE			PrimEx	**HL-LHC?**
		BES III			**Panda**	

a At the wavelength of the emission maximum.
b Top line: slow component, bottom line: fast component.
c Relative light yield of samples of 1.5 X_0 and with the PMT quantum efficiency taken out.
d At room temperature.

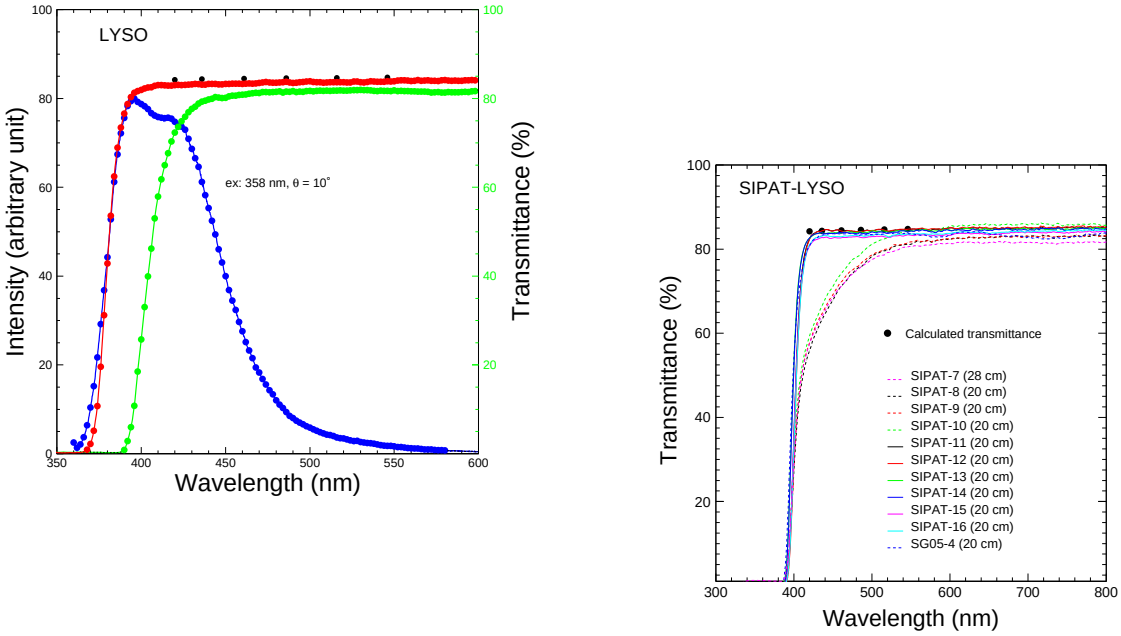

Figure 9.8: Left: The longitudinal (green) and transverse (red) transmittance spectra and the photo-luminescence (blue) spectrum are shown as a function of wavelength for a rectangular LYSO sample with a dimension of 2.5 × 2.5 × 20 cm. Right: Longitudinal transmittance spectra are shown as a function of wavelength for eleven LYSO crystals: ten from SIPAT and one from Saint-Gobain. All, except SIPAT-7, are 20 cm long.

During the R&D phase for crystal development poor longitudinal transmittance was observed in some samples [10]. The right plot of Figure 9.8 shows that four samples (SIPAT-7 to SIPAT-10) have poor longitudinal transmittance between 380 nm and 500 nm, showing an absorption band. A further investigation shows that this absorption band is located at the seed end and is caused by point defects [9]. The investigation was further pointed to a bad seed used in their growth, indicating that these point defects are structure related. With rigorous quality control, LYSO crystals grown later at SIPAT (SIPAT-11 to SIPAT-16) show no absorption band at the seed end, as shown in the right plot of Figure 9.8. An increase of light output at about 30% was found after this problem was resolved. It thus is important to include in crystal specifications a requirement to crystal's longitudinal transmittance.

The left plot of Figure 9.9 shows typical quantum efficiencies of a PMT with multi-alkali cathode (Photonis XP2254b) and an APD (Hamamatsu S8664) [11]. Also shown in the figure are the photo luminescence spectra of LSO/LYSO, BGO and CsI(Tl) crystals, where the area under the luminescence spectra is roughly proportional to the corresponding absolute light output. Table 9.4 summarizes the numerical values of the photo luminescence weighted average quantum efficiencies for various readout devices. These numbers can be used to convert the measured photo-electron numbers to the absolute light output in photon numbers.

A significant red component was observed in the γ-ray induced luminescence spectra in the CTI LSO samples, but not in the LYSO samples from other growers [9]. This red component disappeared after a γ-ray irradiation with an accumulated dose of 5×10^3 rad. This is the only significant difference observed between the large size LSO and LYSO samples [9], indicating that LYSO is a preferred choice.

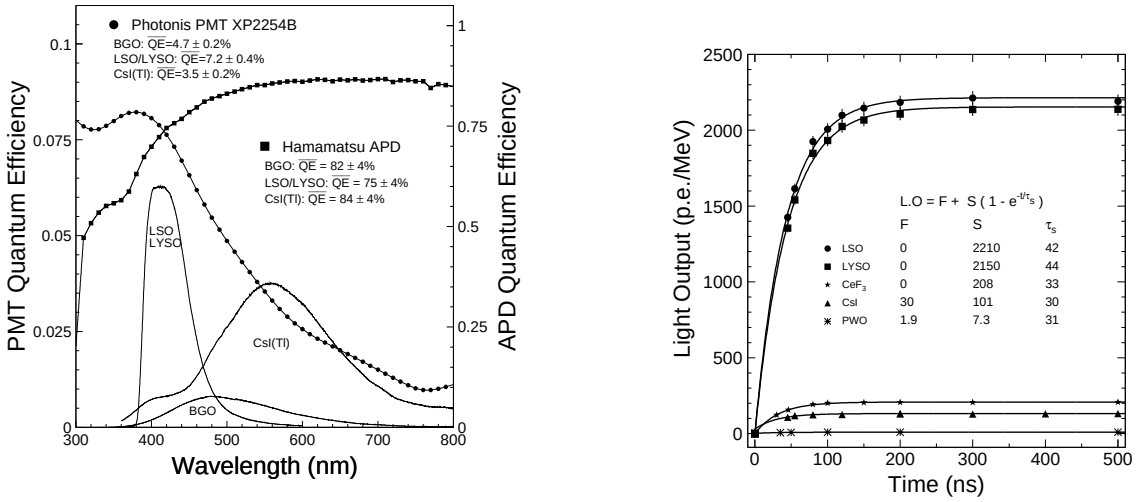

Figure 9.9: Left: The quantum efficiencies of a Hamamatsu R2059 PMT (solid dots) and a Hamamatsu S8664 APD (solid squares)are shown as a function of wavelength together with photo-luminescence spectra of the LSO/LYSO, BGO and CsI(Tl) samples, where the area under the luminescence spectra is roughly propotional to the corresponding absolute light output. Right: Light output measured by using a Photonis XP2254 PMT is shown as a function of integration time for six crystal scintillators.

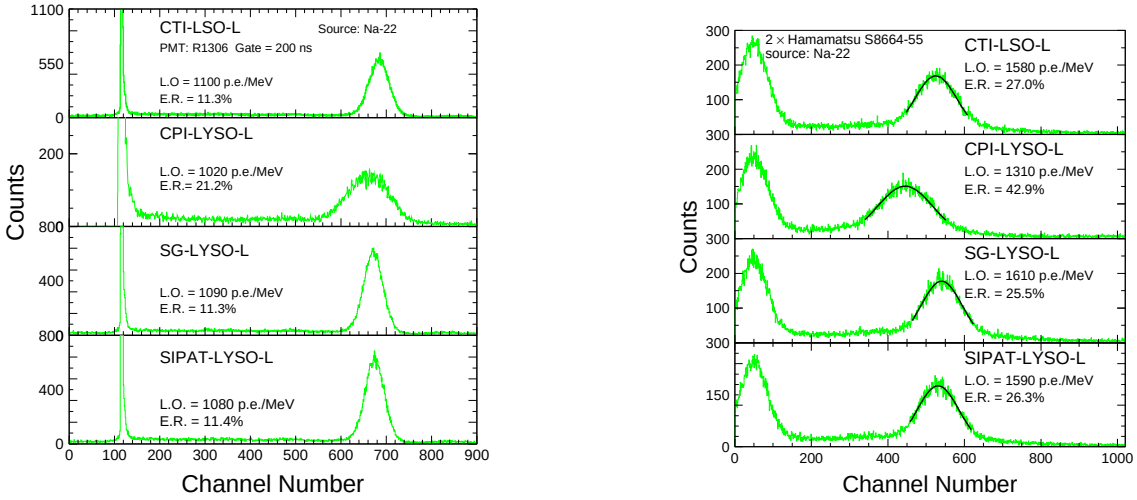

Figure 9.10: 0.511 MeV γ-ray spectra from a ^{22}Na source, measured by a Hamamatsu R1306 PMT (Left) and two Hamamatsu S8664-55 APDs (Right), with a coincidence trigger for four long LSO and LYSO samples of $2.5 \times 2.5 \times 20$ cm^3.

9.3.4.2 Decay time and Light Output

The right plot of Figures 9.9 shows light output in unit of photo-electron/MeV, measured by using a Photonis XP2254 PMT as a function of integration time, for six crystal scintillators [3]. The light output can be fit to the following function to determine the fast and slow components and the decay kinetics:

$$LO(t) = F + S(1 - e^{-t/\tau_s}), \qquad (9.1)$$

where F is the fast component of the scintillation light with a decay time of less than 10 ns, and S represents the slow component with a decay time of τ_s longer than 10 ns. It is clear that the decay time of both LSO and LYSO crystals is at a level of about 40 ns.

As shown in Table 9.3 LSO and LYSO crystals have high light output. It is about 85% and 50% of NAI(Tl) and CsI(Tl) respectively, and is about 18, 4 and more than 200 times of pure CsI, BGO and PWO, respectively. Figure 9.10 shows 0.511 γ-ray pulse height spectra measured by a Hamamatsu R1306 PMT (left) and two Hamamatsu S8664-55 APDs (right) for four LSO and LYSO samples of $2.5\times2.5\times20$ cm^3 from CTI, CPI, SG and SIPAT. The corresponding noise for the APD readout is less than 40 keV equivalent [11]. Poor energy resolution was found in the CPI LYSO sample, but not other samples. According to the grower this was caused by intrinsic non-uniformity which may be improved by appropriate thermal annealing.

It thus is important to include in crystal specifications a requirement to crystal's energy resolution.

Because of their fast decay time and high light output, LSO and LYSO crystals have also been used in time of flight (TOF) measurements for medical applications, such as TOF PET(positron emission tomography). A better than 500 ps FWHM time resolution was achieved for the time difference between two photons. In HEP experiments a rms time resolution of better than 150 ps may be achieved for TOF measurements for single particles. Since the intrinsic rising time of scintillation light is about 30 ps for LSO and LYSO crystals [14], the measured time resolution for LSO and LYSO is affected mainly by the response speed of the readout device and the choice of time pick-off [13]. Doping calcium in LSO and LYSO is reported to reduce the decay time to about 20 ns [15], which would help to improve the time resolution.

9.3.5 Light Collection and Response Uniformity

It is well known that adequate light response uniformity along the crystal length is key for maintaining the precision offered by a total absorption crystal calorimeter at high energies [16]. The light response uniformity of a long crystal as shown in Figure 9.11 (Left) is parameterized as a linear function

$$\frac{LY}{LY_{mid}} = 1 + \delta(x/x_{mid} - 1), \qquad (9.2)$$

where (LY_{mid}) represents the light output measured at the middle point of the crystal, δ represents the deviation from the flat response and x is the distance from the photo-detector. To achieve good energy resolution, the corresponding $|\delta|$ value for SuperB LYSO crystals of 18 X_0 must be kept to less than 3% [17].

Effective light collection requires good light reflector. The glass fiber based supporting structure designed for the superB forward calorimeter is coated with a thin layer of aluminum as reflector. All measurements and simulations discussed in this section are carrired out with aluminum coated glass fiber supporting structure cell, referred to as RIBA Cell, around the crystal.

The light response uniformity of a long tapered LSO/LYSO crystal is affected by three factors. First, the tapered crystal geometry leads to an optical focusing effect, i.e. the response for scintillation light originated at the small end far away from the photo-detector would be higher as compared to that at the large end which is coupled to photo-detector. This is caused by the light propagation inside the crystal, and is common for all optical objects with such geometry. Second, there is a self-absorption effect in LSO/LYSO crystals as discussed in section 9.3.4.1 since a part of the emission spectrum is self-absorbed in the crystal bulk as shown clearly in the left plot of Figure 9.8. This effect is specific for LSO/LYSO crystals. Last, there is a non-uniform light yield along the longitudinal axis of the crystal. It is caused by the segregation process of the cerium activator in LSO/LYSO crystals during the growth. Because of the small segregation coefficient (about 0.2) the cerium concentration increases from the seed end to the tail end of the crystal. Such effect is common for all crystals doped with activator, e.g. CsI(Tl).

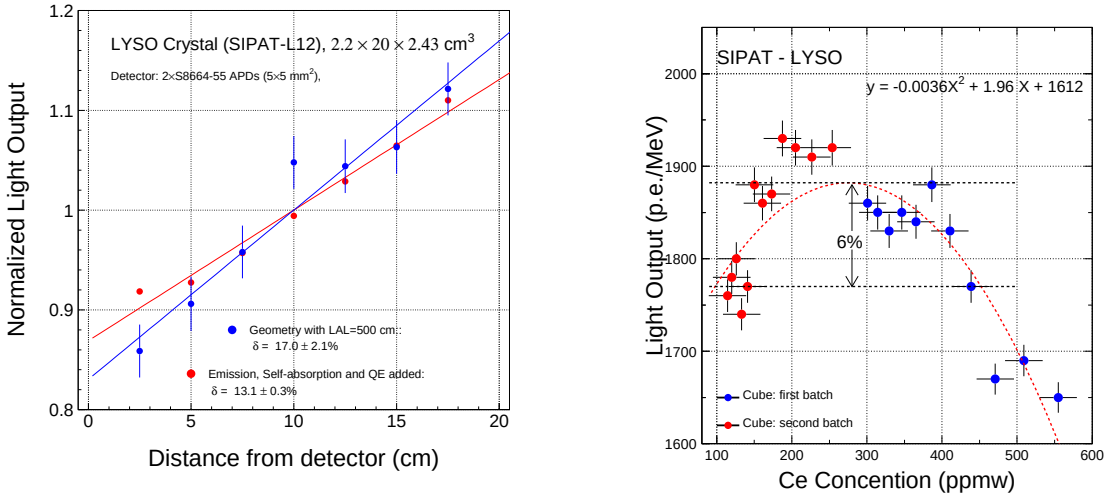

Figure 9.11: Left: Light response uniformities without (blue) and with (red) self-absorption effects, calculated by a ray-tracing program, are shown for a 20 cm long crystal with tapered geometry with two Hamamatsu S8664-55 APD readout. Right: Light outputs measured for 17 mm LSO/LYSO crystal cubes are shown as a function of the cerium concentration.

The left plot of Figure 9.11 shows the light response uniformities calculated using a ray-tracing program [16] for a SuperB LYSO crystal with tapered geometry and two Hamamat S8664-55 APD readout. While the blue dots show the uniformity with only the optical focusing effect the red dots show the same with the self-absorption effect also included. Numerically, the optical focusing effect alone causes a δ value of 17%, which is reduced to 13% with the self-absorption effect included. This indicates that the self-absorption effect provides a partial compensation for the optical focusing effect. The right plot of Figure 9.11 shows the light output measured for two batches of 17 mm LSO/LYSO crystal cubes (red and blue) as a function of the cerium concentrations determined by Glow Discharge Mass Spectroscopy (GDMS) analysis. It shows that the optimized cerium doping level is between 150 and 450 ppmw because of the interplay between the cerium activator density and the self absorption caused by the over-doping. Also shown in the plot is a second order polynomial fit. By adjusting the cerium doping the light yield difference along the crystal can be minimized. A difference at the level of 10% is more or less the maximum, which may provide a variation of the δ value up to 5%. Taking this into account the initial δ value of the SuperB LYSO crystals may vary between 8% to 18%.

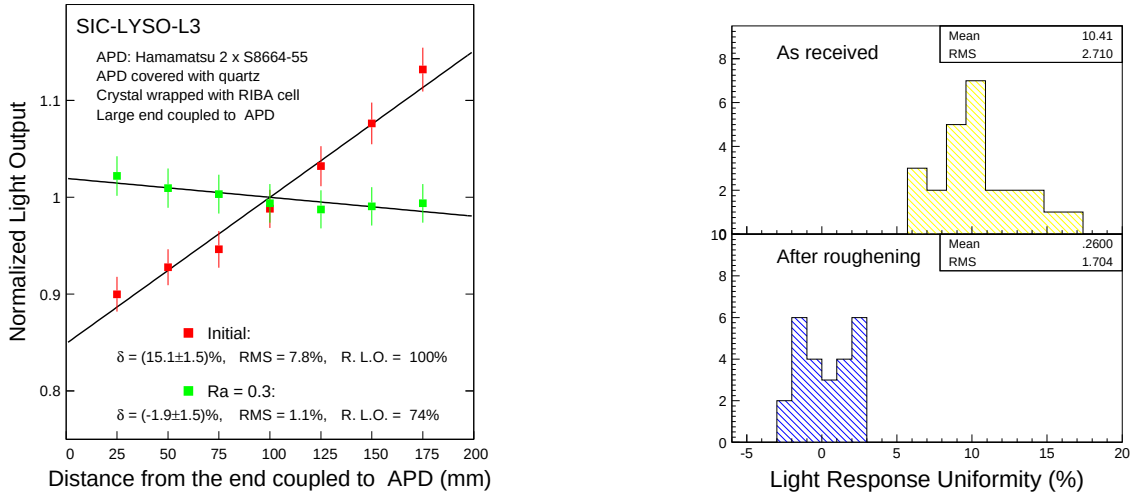

Figure 9.12: Left: Light response uniformity measured with two Hamamatsu S8664-55 APD readout for a tapered SuperB LYSO crystal SIC-L3 before (red dots) and after (green dots) uniformization by roughening the smallest side surface to Ra = 0.3. Right: The distributions of light response uniformity (δ values) are shown for 25 SuperB test beam crystals before (top) and after (bottom) uniformization by roughening the smallest side surface.

Following the experiences of previous crystal calorimeters, such as L3 BGO and CMS PWO, a $|\delta|$ value of less than 3% may be achieved by roughening one side surface of the crystal to an appropriate roughness [18]. The left plot of Figure 9.12 shows the light response uniformities measured with two Hamamatsu S8664-55 APD readout for a tapered SuperB LYSO crystal SIC-L3. The δ value is reduced from 15% before (red) to -1.9% after (blue) roughening the smallest side surface to Ra = 0.3. The right plot of Figure 9.12 shows a comparison of the δ values before (top) and after (bottom) roughening for all 25 SuperB test beam crystals, showing a reduction of the average δ value from 10% to 0.26%. All 25 $|\delta|$ values after uniformization are within 3%. The reduction of light collection efficiency caused by this uniformization is about 17%. It is expected that one or maximum two Ra values would be sufficient to uniformize mass produced LYSO crystals to achieve $|\delta|$ values of less than 3%.

9.3.6 Radiation Hardness

The radiation hardness of long LSO and LYSO samples was investigated against γ-rays [19, 20] and neutrons [21]. It was found that the scintillation mechanism of this material is not damaged, its damage can be completely eliminated by thermally annealed at 300°C and does not recover at room temperature, indicating no dose rate dependence [16]. Studies also show that it is also more radiation hard against charged hadrons [22] than other crystals.

Figure 9.13 shows the longitudinal transmittance (left) and normalized average light output (right) for four 20 cm LSO and LYSO samples from CTI, CPI, SG and SIPAT. The light output was measured by using a XP2254 PMT (top) and two S8664-55 APDs (bottom). All samples tested have a consistent radiation resistance, with degradations of the emission-weighted longitudinal transmittance (EWLT) and the light output of approximately 12% for a γ-ray dose of 1 MRad. This radiation hardness is much better than other scintillation crystals, such as BGO, CsI(Tl) and PWO.

Recently, a 28 cm (25 X_0) LYSO crystal (SIPAT-LYSO-L7) was grown at SIPAT. This LYSO sample has consistent emission, adequate light response uniformity and good radiation hardness against γ-rays up to 1 Mrad [10]. The left plot of Figure 9.14 shows the pulse height spectra measured by a Hamamatsu R1306 PMT at seven points evenly distributed along SIPAT-LYSO-L7. The FWHM resolutions obtained for 0.511 MeV γ-rays from the ^{22}Na source are about 12.5%. This is quite good for crystals of such length. The right plot of Figure 9.14 shows normalized light output and response uniformity measured by two Hamamatsu S8664-55 APD before and after γ-ray irradiations with an integrated dose of 10^2, 10^4 and 10^6 rad. The degradation of the light output was found to be about 13% after 1 Mrad dose. The light response uniformity of SIPAT-LYSO-L7 does not change even after 1 Mrad dose, indicating that its energy resolution may be maintained [16].

In a brief summary, LSO and LYSO crystals are radiation hard crystal scintillator. Because of their excellent radiation hardness these crystals are expected to find applications in an environment where severe radiation environment is expected.

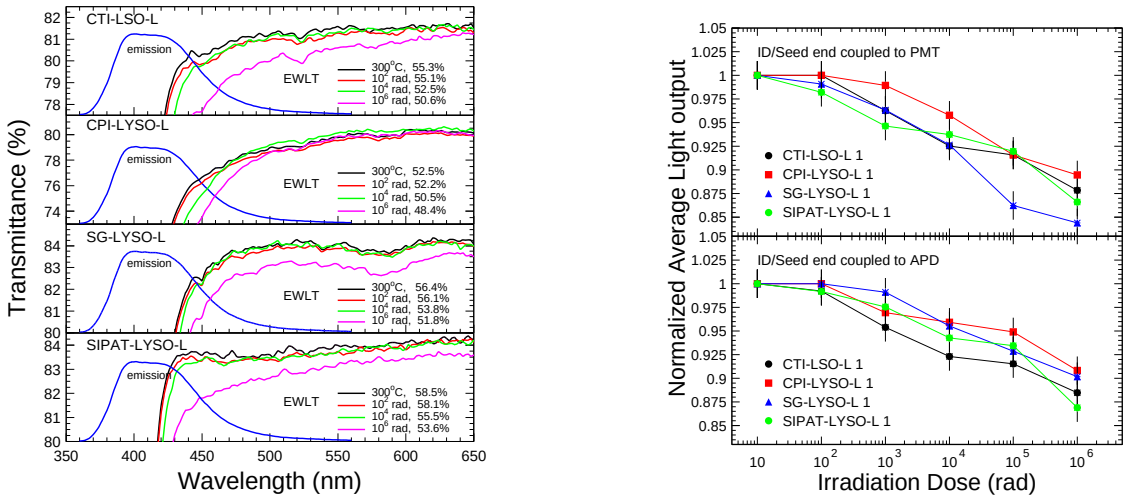

Figure 9.13: The longitudinal transmittance spectra in an expanded view (left) and the normalized light output (right) are shown as a function of the integrated dose up to 1 Mrad for four LSO and LYSO samples of $2.5 \times 2.5 \times 20$ cm^3. Also shown in the left plot is the photo-luminescence spectra (blue) in arbitrary unit.

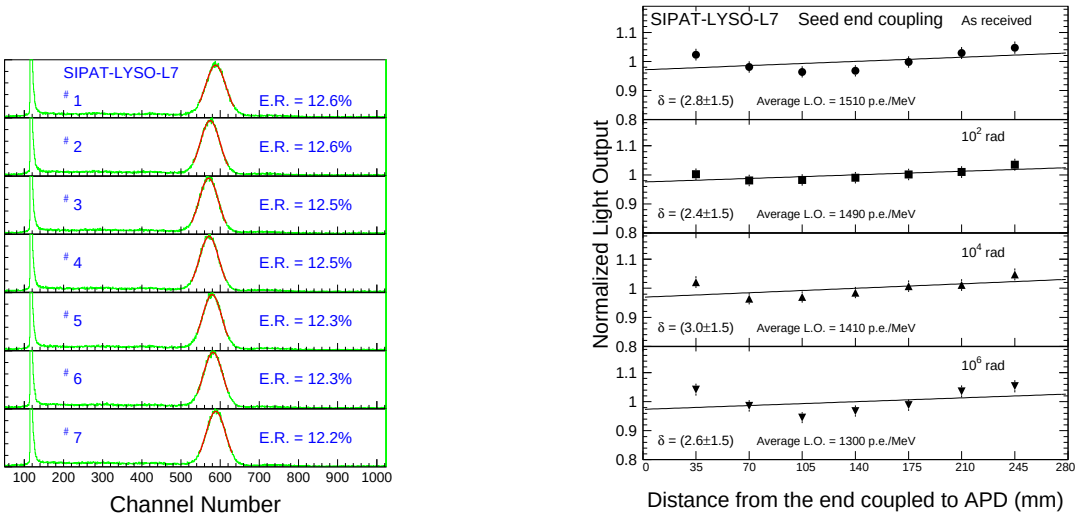

Figure 9.14: Left: The pulse height spectra of 0.511 MeV γ-ray peaks (green) and corresponding Gaussian fits (red) measured by a Hamamatsu R1306 PMT are shown at seven points evenly distributed along SIPAT-LYSO-L7. Also shown are the numerical values of the FWHM energy resolutions (E.R.). Right: Normalized light output and light response uniformity measured by two Hamamatsu S8664-1010 APDs, before and after γ-ray irradiations in several steps up to 1 Mrad are shown for SIPAT-LYSO-L7.

9.3.7 Specifications, Production and Testing

Following our extensive R&D on LYSO crystals, the following specifications are defined for the procurement of high quality LYSO crystals ffrom various vendors for the SuperB forward calorimeter.

- Dimension: +0.0/-0.1 mm.
- Longitudinal transmission at 420 nm: $>$ 75%.
- FWHM energy resolution: $<$ 12.5% for 0.511 MeV γ-rays measured by a Hamamatsu R1306 with DC-200 coupling at 7 points along the crystal.
- Light output will be required to be more than a defined percentage of a small crystal candle with air-gap coupling to PMT.
- Light Response uniformity ($|\delta|$): $<$ 3% measured by two Hamamatsu S8864-55 APDs.

Crystals will be produced by various vendors. The total crystal volume for the SuperB forward calorimeter is 0.36 m^3, which is small as compared to LYSO crystals grown for the medical industry. The following instruments are needed at each of the crystal vendors as well as the SuperB crystal laboratory.

- A station to measure crystal dimension.
- A photo-spectrometer with large sample compartment to measure the longitudinal transmission along 20 cm path.
- A PMT based pulse height spectrometer to measure light output and FWHM energy resolution with 0.511 MeV γ-rays from a ^{22}Na source.
- An APD based pulse height spectrometer to measure light response uniformity with 0.511 MeV γ-rays from a ^{22}Na source.

Table 9.4: Photo Luminescence Weighted Quantum Efficiencies (%)

Photo Luminescence	LSO/LYSO	BGO	CsI(Tl)
Hamamatsu R1306 PMT	12.9±0.6	8.0±0.4	5.0±0.3
Hamamatsu R2059 PMT	13.6±0.7	8.0±0.4	5.0±0.3
Photonis XP2254b	7.2±0.4	4.7±0.2	3.5±0.2
Hamamatsu S2744 PD	59±4	75±4	80±4
Hamamatsu S8664 APD	75±4	82±4	84±4

Bibliography

[1] C. Melcher and J. Schweitzer, "Cerium-doped lutetium oxyorthosilicate: a fast, efficient new scintillator," *IEEE Trans. Nucl. Sci.* **39** (1992) 502–505.

[2] D.W. Cooke, K.J. McClellan, B.L. Bennett, J.M. Roper, M.T. Whittaker and R.E. Muenchausen, "Crystal Growth and Optical Characterization of Cerium-doped $Lu_{1.8}Y_{0.2}SiO_5$," *J. Appl. Phys.* **88** (2000) 7360–7362, and T. Kimble, M Chou and B.H.T. Chai, "Scintillation Properties of LYSO Crystals," in *Proc. IEEE Nuclear Science Symposium Conference* (2002).

[3] R.H. Mao, L.Y. Zhang and R.-Y. Zhu, "Optical and Scintillation Properties of Inorganic Scintillators in High Energy Physics," *IEEE Trans. Nucl. Sci.* **NS-55** (2008) 2425–2431.

[4] W. Wisniewski, "Consideration for Calorimetry at a Super B Factory", in *Proceedings of Tenth International Conference on Calorimetry in Particle Physics*, Ed. R.-Y. Zhu, World Scientific (2002), and C. Cecchi. "A LYSO Calorimeter for a SuperB Factory ," in *Proceedings of Fourteenth International Conference on Calorimetry in Particle Physics*, Journal of Physics Series (2010).

[5] F. Happacher, "CCALT: Crystal Calorimeter at KLOE2," in *Proceedings of Fourteenth International Conference on Calorimetry in Particle Physics*, Journal of Physics Series (2010).

[6] The Mu2e Experiment, see http://mu2e.fnal.gov/.

[7] R.-Y. Zhu, Talk given at the CMS Forward Calorimetry Task Force Meeting at CERN, June 17, 2010. See http://indico.cern.ch/getFile.py/access?sessionId=0&resId=4&materialId=0&confId=97272

[8] D.A. Ma and R.-Y. Zhu, "Light Attenuation Length of Barium Fluoride Crystals," *Nucl. Instr. and Meth.* **A333** 422-424 (1993).

[9] R.H. Mao, L.Y. Zhang and R.Y. Zhu., "Emission Spectra of LSO and LYSO crystals Excited by UV Light, X-ray and γ-ray," *IEEE Trans. Nucl. Sci.* **55** (2008) 1759–1766.

[10] Rihua Mao, Liyuan Zhang and Ren-yuan Zhu, "Quality of a 28 cm long LYSO Crystal and Progress on Optical and Scintillation Properties," Paper N38-2 in *2010 IEEE NUCLEAR SCIENCE SYMPOSIUM CONFERENCE RECORD.*

[11] J.M. Chen, L.Y. Zhang and R.-Y. Zhu, "Large Size LSO and LYSO Crystal Scintillators for Future High Energy Physics Experiments," *IEEE Trans. Nucl. Sci.* **NS-54** (2007) 718–724 and *Nucl. Instr. and Meth.* **A572** (2007) 218–224.

[12] J.M. Chen, L.Y. Zhang and R.-Y. Zhu, "Large Size LYSO Crystals for Future High Energy Physics Experiments," *IEEE Trans. Nucl. Sci.* **NS-52** (2005) 3133–3140.

[13] R.-Y. Zhu, Invited talk given at the Time Resolution Workshop at University of Chicago, April 28, 2011. See http://www.hep.caltech.edu/∼zhu/talks/ryz_110428_t

[14] S.E. Derenzo, M.J. Weber, W. W. Moses, and C. DuJardin, "Measurements of the Intrinsic Rise Times of Common Inorganic Scintillators," *IEEE Trans. Nucl. Sci.* **47** (2000) 860–864.

[15] T. Szczesniak, M. Moszynski, A. Synfeld-Kazuch, L. Swiderski, M.A.S. Koschan and C.L. Melcher, "Time resolution and decay time of LSO Crystals Co-Doped with Calcium," *IEEE Trans. Nucl. Sci.* **57** (2010) 1329–1334.

[16] Ren-yuan Zhu, "Radiation Damage in Scintillating Crystals," *Nucl. Instr. and Meth.* **A413** (1998) 297–311.

[17] *The CMS Electromagnetic Calorimeter Project*, CERN/LHCC 97-33 (1997).

[18] Rihua Mao, Liyuan Zhang and Ren-yuan Zhu, "Optimization of Light Response Uniformity for SuperB Tapered LYSO Crystals with APD Readout," Paper N2 *2011 IEEE NUCLEAR SCIENCE S POSIUM CONFERENCE RECORD*.

[19] J.M. Chen, R.H. Mao, L.Y. Zhang R.Y. Zhu, "Gamma-ray induced radi damage in large size LSO and LYSO tal samples," *IEEE Trans. Nucl. Sci* (2007) 1319–1326.

[20] Rihua Mao, Liyuan Zhang and yuan Zhu, "Gamma-ray induced radi damage in PWO and LSO/LYSO tals," *2009 IEEE NUCLEAR SCIE SYMPOSIUM CONFERENCE REC* VOLS 1-5 (2009) 2045-2049.

[21] Rihua Mao, Liyuan Zhang and Ren- Zhu, "Effects of neutron irradiations i ious crystal samples of large size fo ture crystal calorimeter," *2009 IEEE CLEAR SCIENCE SYMPOSIUM FERENCE RECORD*, VOLS 1-5 (2041-2044.

[22] F. Nessi-Tedaldi, G. Dissertori, Lecomte, D. Luckey and F. P "Studies of Cerium Fluoride, LYSO and Lead Tungstate Crystals Exposed to High Hadron Fluences," Paper N32-3, 2009 IEEE NSS Conference.

9.3.8 Readout and Electronics[VB]

9.3.8.1 APD Readout[DH]

The photosensors chosen for readout of the LYSO crystals of the forward endcap are an independent pair of 10×10 mm avalanche photodiodes (APDs). The APDs have several advantages over photodiodes in this application: they are a better match to the emission spectrum of LYSO, providing a quantum efficiency integrated over the spectrum of 75% (see Figure 9.15); they provide useful gain (of the order of 75) with low noise; and, as they have a thinner sensitive region, they suffer less from the nuclear counter effect.

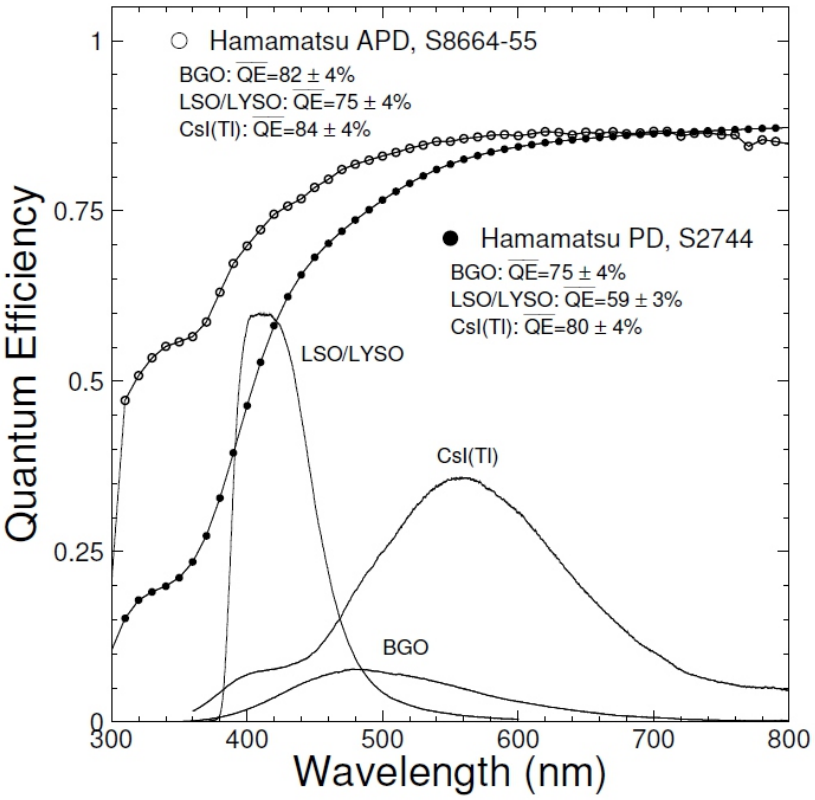

Figure 9.15: Quantum efficiency of a Hamamatsu APD and photodiode, together with the emission spectra of LYSO, BGO and CsI(Tl) crystals.

The gain with low noise of the APDs presents two additional advantages: it can allow a reduction of the shaping and integration time constants, constants that, as shown in Sec. 9.3.1, can be used as a handle to fight the machine background; it improves the signal-to-noise ratio for the signals used for calibration (see Sec. **??**), allowing a crystal by crystal calibration (see Sec. 9.3.9).

9.3.8.2 Electronics Block diagram

9.3.8.3 Preamplifier

9.3.8.4 Shaper

9.3.8.5 Digitization

9.3.8.6 Requirements on mechanics

Cables, encumbrances, required cooling, ...

9.3.9 Calibrations[DH]

9.3.9.1 Initial calibration with source

A goal of the design is that the signal rate and the signal-to-noise ratio with a typical radioactive source such as ^{137}Cs be sufficient to allow individual calibration of each crystal with the readout device with which it will actually be paired. Photodiode readout of large crystals does not allow the use of sources for calibration and setup; this is typically done with a reference photomultiplier, with the results then convoluted with the results of individually calibrated photosensors. Such a procedure does not,of course, fully account for the effects of surface oxidation of the crystal or glue joint losses. With APD readout, the response of the entire chain can be measured.

The full setup of each crystal assembly requires each crystal/readout package to be individually adjusted to meet the uniformity requirements *in situ* and the characteristics of each object to be entered into a reference database. This involves appropriate roughening of, typically, one crystal surface to conform to a light collection uniformity specification ($\sim \pm 5\%$ over the forward 90% of each crystal) formulated to meet the energy resolution specification. The output of this setup/calibration procedure is then entered into a reference database, which serves as the initial set of calibration constants for the calorimeter system.

The fully assembled calorimeter is then calibrated with the circulated fluorinert system already used in BaBar (see Sec. 9.2.7) at appropriate intervals (one to four weeks in the case of *BABAR*). A substantial advantage of this approach is that there is an individual pedestal and gain constant for each crystal. A limitation is that the source is at a relatively low energy, although it is at a higher energy than that obtained from long-lived radioactive sources. This can be a problem in particular if using crystals with intrinsic radioactivity, such as for instance the LYSO. For such a crystal the calibration system needs to be properly designed to achieve the required accuracy in a sustainable time.

Calibration with radiative Bhabhas can overcome this limitation, but it requires development of a complex matrix unfolding procedure, since high energy electrons deposit shower energy in many crystals, not in a single crystal as in the case of source calibration.

9.3.9.2 Electronics calibration

9.3.9.3 Temperature monitoring and correction

The characteristics of APDs place fairly stringent requirements on the temperature control of the system, greater than those imposed by the temperature variation of light output of the crystals, as well as on the stability of the APD power supply voltage.

The Hamamatsu S-8664 APDs specified for the crystal readout have a temperature coefficient of gain of $\Delta G/\Delta T$ of 2.5%/°C, while the LYSO light output varies $-0.2\%/°C$. A specification of an APD gain stability of $\pm 0.5\%$ requires knowledge of the temperature to $\pm 0.2°C$. The CERN beam test demonstrated that a measurement of the calorimeter temperature to 0.2°C can be easily achieved. Furthermore the energy degradation due to machine background might allow to tolerate even a less stringent control.

As far as the overall structure is concerned we can keep the characteristics of the BaBar one. The entire calorimeter is surrounded by a double Faraday shield composed of two 1mm-thick aluminum walls, so that the diodes and preamplifiers are shielded from external noise. Such shield also served as an environmental enclosure, surrounding the slightly hygroscopic CsI(Tl) crystals with a dry, temperature controlled nitrogen atmosphere. The preamplifiers (2 50mW/crystal) and the digitizing electronics (∼3 kW per end-flange) were the primary internal heat sources. The temperature was monitored by 256 thermal sensors distributed over the calorimeter. This system maintained the crystal environment at $20 \pm 0.5°C$. Dry nitrogen circulation stabilizes the relative humidity at $1 \pm 0.5\%$. This system can be extended to a forward endcap in a straightforward manner.

As far as gain stability is concerned, a gain of ∼75, with a reverse bias voltage of ∼375V, a voltage stability of better than 1 volt is required. This requirement can be met by commercially available computer-controlled high voltage supplies, such as those used for the CMS calorimeter.

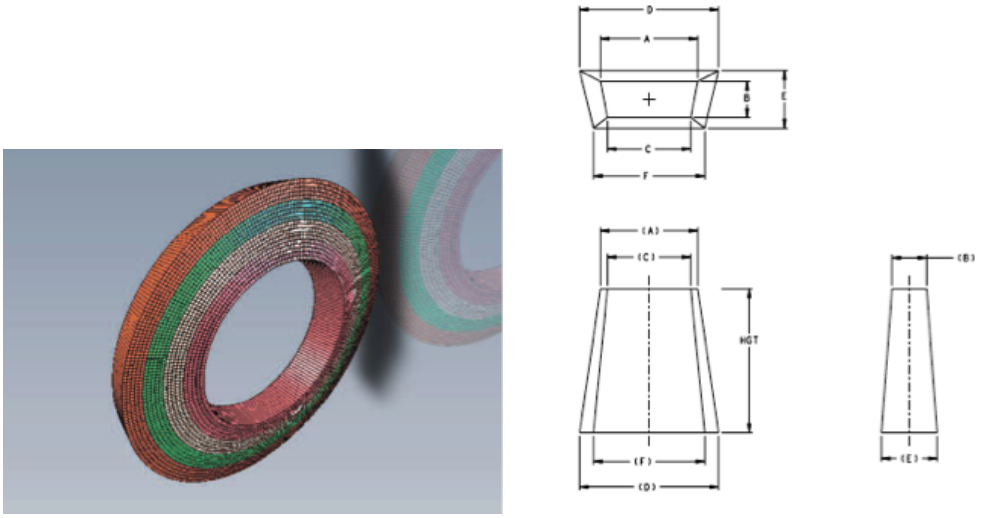

Figure 9.16: Left: overview of the structure of the FWD EMC. Right: definition of the sides of the crystals.

Ring	A	B	C	D	E	F	Front radius	Front Z	Back radius	Back Z	Angle	Crystals/Ring	Modules/Ring
1	17,99	21,38	17,27	19,9	23,84	19,1	516,5027	1977,9057	570,1961	2170,5634	15,57	180	36
2	18,69	21,41	17,98	20,69	23,88	19,89	536,7307	1969,3528	592,7885	2161,336	16,28	180	36
3	19,4	21,44	18,68	21,48	23,91	20,68	556,9553	1960,8002	615,3755	2152,0777	16,98	180	36
4	20,1	21,46	19,39	22,27	23,94	21,47	577,1766	1952,248	637,956	2142,789	17,69	180	36
5	20,81	21,48	20,1	23,05	23,96	22,26	597,3946	1943,6962	660,5288	2133,47	18,4	180	36
6	18,39	21,5	17,78	20,38	23,98	19,7	617,7018	1935,1066	683,1854	2124,0826	19,11	210	42
7	18,99	21,51	18,38	21,05	24	20,38	637,9132	1926,5562	705,7396	2114,704	19,82	210	42
8	19,59	21,52	18,99	21,73	24,01	21,05	658,1213	1918,0067	728,2829	2105,2962	20,54	210	42
9	20,2	21,53	19,59	22,4	24,02	21,73	678,3261	1909,4581	750,814	2095,8595	21,25	210	42
10	20,8	21,53	20,2	23,07	24,02	22,4	698,5278	1900,9106	773,3321	2086,3946	21,96	210	42
11	18,68	21,53	18,16	20,73	24,02	20,15	718,8334	1892,3616	795,9432	2076,8991	22,68	240	48
12	19,21	21,53	18,69	21,32	24,02	20,74	739,1376	1884,0674	818,5408	2067,6297	23,39	240	48
13	19,74	21,53	19,22	21,91	24,02	21,33	759,4449	1875,7717	841,1283	2058,3307	24,11	240	48
14	20,27	21,52	19,76	22,5	24,01	21,93	779,7553	1867,4744	863,7047	2049,0026	24,82	240	48
15	20,8	21,51	20,29	23,08	23,99	22,52	800,0686	1859,1756	886,2689	2039,6458	25,53	240	48
16	18,9	20,52	18,47	20,98	23	20,5	820,0635	1851,1039	908,4988	2030,4895	26,24	270	54
17	19,35	20,5	18,92	21,48	22,98	21,01	839,5277	1843,2795	930,181	2021,5545	26,95	270	54
18	19,8	20,48	19,38	21,99	22,95	21,51	858,9945	1835,4532	951,8474	2012,5925	27,66	270	54
19	20,25	20,45	19,83	22,49	22,92	22,02	878,4639	1827,6249	973,497	2003,6042	28,37	270	54
20	20,7	20,43	20,29	22,99	22,89	22,52	897,9357	1819,7946	995,1289	1994,5901	29,08	270	54

Figure 9.17: Nominal dimensions of the sides of the crystals. See Fig. 9.16 for the definition of the sides.

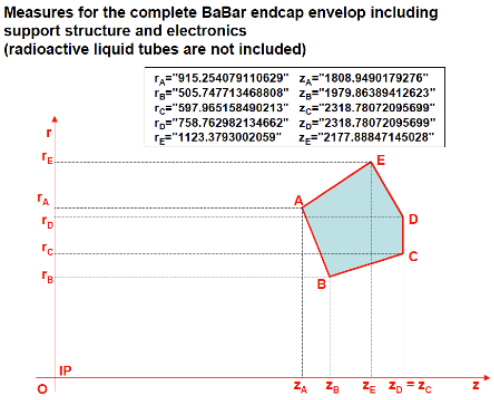

Figure 9.18: FWD EMC envelope.

9.3.10 Mechanical Design[CG]

9.3.10.1 Introduction and parameters

The calorimeter is designed to measure with maximum precision the energy deposited by impinging particles into the crystals. All material out of the crystals is unwelcome because it absorbs a fraction of undetected (unmeasured) energy. Material in front (support shell) and between (cell walls) crystals has to be minimized. Building materials with low-Z molecular composition in limited quantities is favored for this reason. The basic physical requirement to the design of this structure is to ensure a nominal distance between crystal faces of 0.4 mm within a module (gap) and a nominal distance between crystal faces across two modules of 0.6 mm (crack). Finally, crystals should point to the interaction region.

To simplify the design we can exploit both the symmetry in ϕ and the possibility to group the crystals in four rings in theta (see Fig. 9.16 left) each composed of 36,42,48, and 54 modules respectively. The cells, whose dimensions are reported in Fig. 9.17, are designed in order to keep the cell front dimension (B, see Fig. 9.16 right).

9.3.10.2 General contraints and requirements

The EMC forward volume envelope is the one defined by the Babar experiment and reported in Fig. 9.3.10.1. Additional constraints coming from the new requirements for services and access have been considered.

The design of the mechanical structure foresees that the volume devoted to the EMC is divided in two, an alveolar volume and a service volume (see Fig. 9.3.10.2). The definition of this two volumes is based on assembly constraints and is optimized to simplify access to the services. Volumes shape and dimensions are such to allow free insertion of outer row of crystals.

from installation, access and maintenance TBD

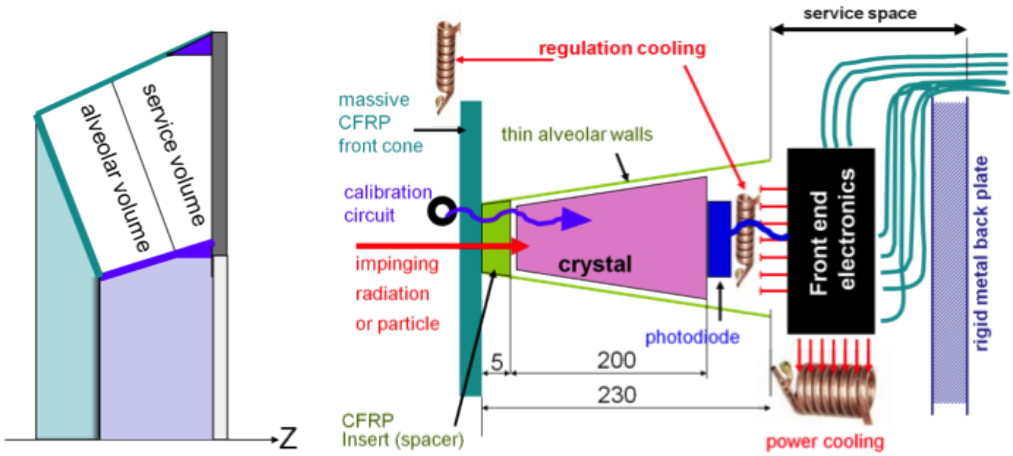

Figure 9.19: FWD EMC volumes and layout

9.3.10.3 Cooling and Calibration requirements

Structural integrity requires any produced heat to be evacuated by a cooling system. As discussed in Sec. 9.3.9 the light / signal conversion factor of the photo-detector (APD) depends on the temperature and requires a thermal regulation. There are two separate thermal volumes: the volume which encloses the crystals and photodetector, where no power dissipation is expected, and the volume comprised between the modules and the backplate, where all the thermal power is dissipated. The cooling is ensured by two active systems. A regulated circuit keeps the operating temperature of the crystal array and of the photodetector within a tight temperature spread ($\pm 0.5^o$C in BaBar). A second cooling circuit evacuates the heat generated by all power sources (front-end electronics) in the space between the modules and the back plate.

A calibration circuit flows a fluid (Fluorinert FC77) activated by a neutron source (see Sec. 9.2.7). The circuit flows past the ECAL front face, thus showering every crystal with calibrated 6,13 MeV γs, with the system shown in Fig 9.20. Under study either the possibility to reuse the BaBar monitoring system or to build a new circuit embedded in the front sandwich plate of the shell structure.

Figure 9.20: calibration circuit at the front of BaBar calorimeter

9.3.10.4 Crystal sub-unit design

The crystal subunit consists of the crystal and the capsule assembly with the photo-detector. Upon delivery crystals are visually inspected, measured and characterized. The crystal tolerance (0.1 mm), the chamfer width (0.7 mm maximum). Crystal chamfers are necessary to ease surface lapping and polishing, avoid edge chipping and ease safe handling, match cell corner radii. Chamfer size has to be small enough to neglect the resulting light losses and maximize photo device interface (e.g. 0.3 - 0.7mm).

9.3.10.5 Module design

Modules contain a 5 x 5 matrix of crystals and therefore their approximated dimensions are 110 x 110 x 230 mm^3 and the total weight of the crystals is about 25kg. The requirements on the thickness and the material of the walls constrain the module to be held in a very light container of 220g, thus making the mechanical requirements challenging.

Physical constraints

As detailed in Sec. 9.3.10.1, modules are assembled in 4 concentric rings containing growing numbers of 5x5 modules. With the ϕ and θ symmetries the number of crystals types that need to be produced is reduced to 20. To achieve the required energy resolution, crystal-to-crystal separation must be less than or equal to half a millimeter. The design guarantees a maximum distance between crystal faces of 0.4 mm within a module and of 0.6 mm across two modules, either in ϕ or in θ for crystal nominal dimensions. For the crystals with the smallest tolerances these values are reduced by 0.1 mm . Inside a module, this distance results from the following contributions (see Fig. 9.21):

- the crystal processing tolerance, from 0 to 0.1 mm.
- a guaranteed air gap between the crystal nominal (maximal) shape and the alveolar container of 0.1 mm to cope with the maximal alveolar unit elastic deformation in the worst case (crystals horizontal) and handling, transport or installation acceleration. Crystals do not take part in the structural resistance of the alveoli.
- the alveolar unit nominal wall thickness of 0.2 mm (including its manufacturing tolerance of 20 ?m). Between two modules, this distance results from the following contributions:
- the crystal processing tolerance from 0 to 0.1 mm,
- the 0.1 mm air gap inside the alveolar unit,
- the two facing walls of 0.1 mm each,
- an additional contribution of 0.35 mm due to the module copper shielding
- the 0.1mm gap between the two modules

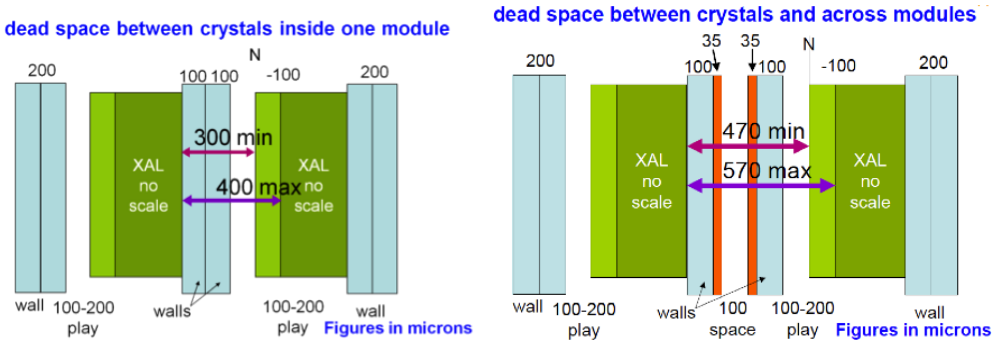

Figure 9.21: crack (crystal to crystal, left picture) and gap (module to module, right picture)

Space is left between modules to make the assembly possible (module dimensional tolerances) for module-to-module mechanical connection insertion of pre-preg fillers

The 5 x 5 modularity is considered an economic optimum (moulding cycle, handling, assembly, etc.) for the production aspects. It is also convenient for general architecture and integration front-end electronics modularity and connection and electromagnetic shielding. A 5x5 data matrices are also used in event reconstruction. A small chamfer on the crystal edges is required because of the fragility of crystals and allows a small inner radius on the cell inside. This chamfer is also very useful for the polishing process.

At the front of the crystal the cell is closed by an insert (see Fig 9.22). The inserts are made of a CFRP with short C fibers in an epoxy matrix. This material is easy to machine and a good match for the insert complex shape. Although more expensive, carbon is preferred to glass as making less material in front of the crystal. It also ensures the electrical continuity with the Cu foil of the module electromagnetic shielding. The insert has a central hole used during alveola production. Few of these holes are used for the final module positioning in the Shell-Module and for the mechanical interface through composite set-pins.

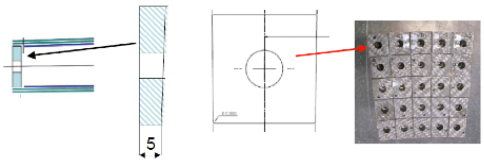

Figure 9.22: CFRP inserts at the front of the alveolar cells

At the opposite side metallic clamps tightened on cell walls keep crystals in position (see Fig 9.23).

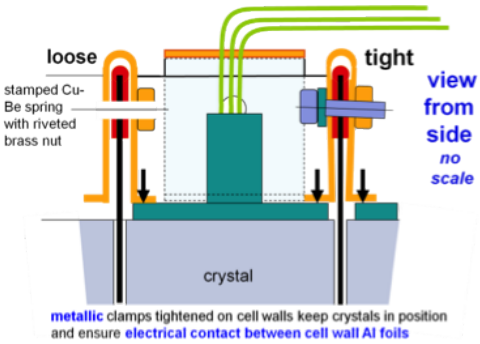

Figure 9.23: metallic clamps hold crystals in position

Grounding and shielding

An aluminum foil inside the cell acts as a reflector for the crystal and provides electromagnetic shielding. The aluminum surface can be optically improved by a special metallic or transparent coating to enhance its reflectivity. Alveolar design must allow electrical contact between all conductive materials the Al reflecting foils of every cell in one alveolar should be electrically connected. Connections are in the cell rear empty space (see Fig 9.24), through holes designed for crystal fixation.

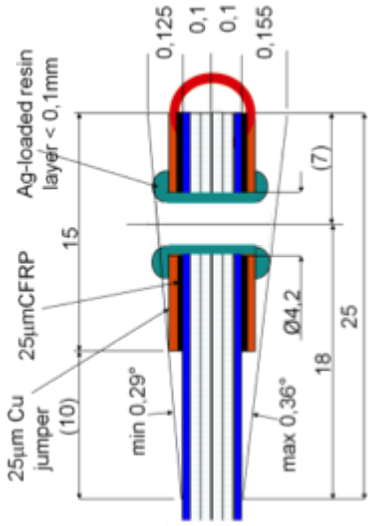

Figure 9.24: detail of the cell back open side

Cell grounding just requires to put all cell Al reflectors in contact. Cell shielding needs additional metal thickness. Alveolar shielding is achieved by an ultimate Cu wrap of 50μm around sides on the external of the module (see Fig 9.25). The Cu foil does not need additional adhesive film thickness as it is cured with the wall prepreg. The price to pay is 100μm more dead space at every module to module transition. A similar foil is merged into the Support Shell bottom plate. The bonded Cu foil, covering the four sides of the alveolar module, is connected to the cell ground.

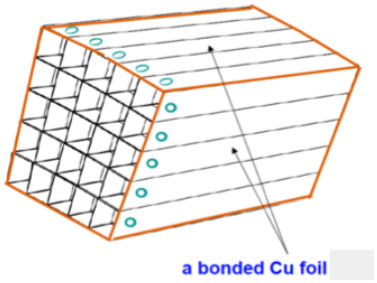

Figure 9.25: Cu foil around the module

Module supporting principles

As described in Fig 9.3.10.5 Alveolar modules are assembled into the Shell-Support-Structure (horse collar and wedge). Alveolar front ends are driven into position by 5 tubular CFRP setpins and the front of the module is glued to the structure front plate.

Alveolar back end sides are glued together via composite in θ. Connection between modules at the back reduces the bending moment of the alveola. Narrow glue strips are used because gluing of complete adjacent module walls is technically impossible. To achieve autoclave gluing of all modules in one operation the resin used for module front and sides has a lower curing temperature than that of the shell and modules. Alveolar unit moulding technique, precision, wall composition, radii and chamfers The alveolar container of a module is moulded in a precision CNC machined aluminium mould (tolerance of 0.02 mm) consisting of a box and a cover, and 25 mandrels (Fig 9.27) with shapes similar to those of crystals.

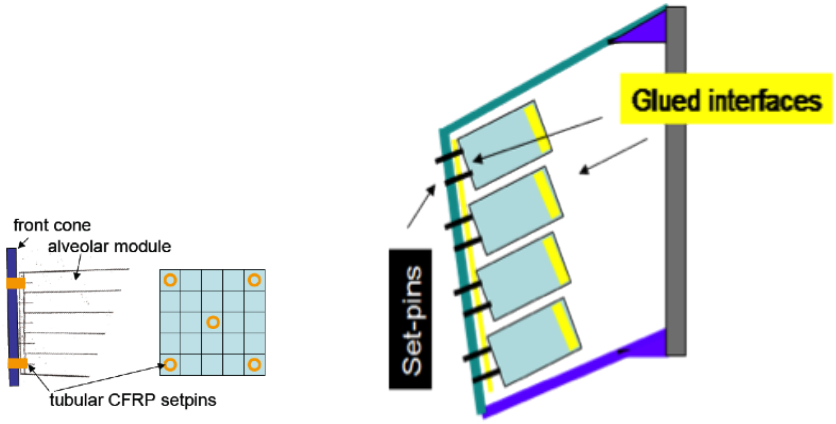

Figure 9.26: Alveola supports

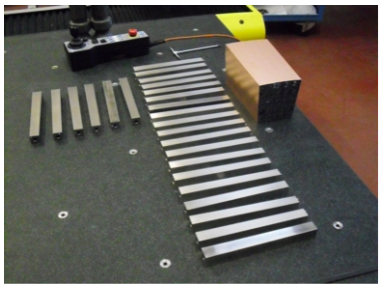

Figure 9.27: Alveolar module mandrels

The wall layers described next are wrapped around the mandrels. The mandrels are positioned with accurate setpins in precision holes of the mould box. A 50μm Cu layer is wrapped all around the module before closing the mould. Closing the mould cover presses the layers together and keeps the mandrels position with high accuracy. The moulding method requires a very uniform distance between the mandrels and the mould cavity in order to balance the very high pressures exerted when closing the mould and curing the resin. This is achieved by giving the mandrel the crystal theoretical shape increased by 0.1 mm (clearance between crystal and alveolar cavity).

The assembly (Fig 9.28) is taken to the autoclave to cure the resin. This curing is performed at 120 for 90 minutes, plus the time to reach the curing temperature and to cool down. A finishing of the ends of the module is performed after the extraction of the mandrels.

The wall of the alveola is described in Fig. 9.29. The first layer consists of an aluminium foil of a thickness of 25 μm and has a triple function. It rigidifies the alveolar unit, acts as a reflector for the crystal and provides electromagnetic shielding. The aluminum surface can be optically improved by a special metallic or transparent coating to enhance its reflectivity. The second layer consists of a glass fibre epoxy resin prepreg of a thickness of 75 μm. The 75 microns is obtained by the wrapping of two layers, 35 microns, of FGRP (Fiber Glass Reinforced Plastic). This material has been selected for its ability to produce very thin walls with a very small radius of curvature. Given wall thickness and radius limit, the combination of fibre material and diameter is such to avoid edge breaking at moulding and ensure cell structure integrity.Glass fibre is also very economical and easy to process. The 0.02 mm accuracy of the moulding is consistent with the alveolar unit tolerances. The total thickness of glass fibre wrapped around a mandrel is nominally 100 microns. The resulting surface density of material between two crystals is 200 g/m2. No other material can produce walls thin enough to maintain the gap between crystals to 0.4 mm. Compared to carbon-fibre, glass fibre has a relatively low elasticity modulus and can be formed with a sharper bending radius. Mandrels producing the inner shape are chamfered at 0.3 mm ? 45.

Module Prototypes

To validate the submodule design, two prototypes of the alveola module have been constructed (see the photos in Fig. 9.29).

A first prototype (Proto1) was produced to validate the cell structure concept and the production economy It was then used with its 25 crystals in a beam of particles for physics validation The Proto1 validated the whole production process and a 3D dimensional inspection performed on the internal and external walls gave evidence of the achievable dimensional tolerances. Wall thickness was measured at the cell open edge over 20mm depth on both sides of punched holes and produced the following values : a) for internal walls nominal 0,200mm 0,15 to 0,22 b) for external walls nominal 0,135mm 0,13 to 0,17

The information gathered have been used to define the production protocol.

Figure 9.28: alveolar module production process

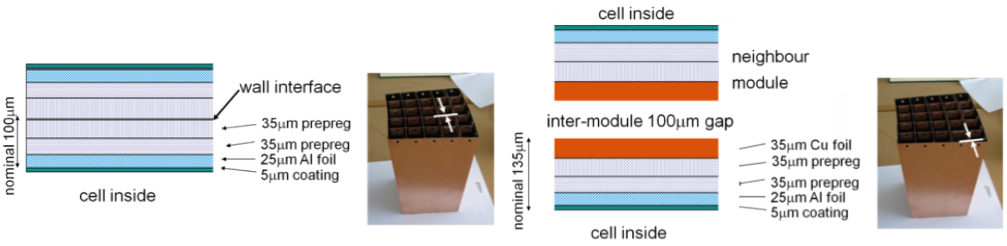

Figure 9.29: Alveolar module walls internal and external

A second prototype (Proto2) was produced in September 2011 to confirm process repeatability and to evaluate the global mechanical properties of the structure.The alveolar module is identical to that used for the physics beam test in October 2010, Proto1. The test campaign had the aim to evaluate the structure overall mechanical properties. Global deformations of the alveolar array are significant, and a loading test is essential for checking the absence of interference with the shell inside (inner and outer cone) and the absence of crystal stressing (cell bending ¡ play) in a first approximation. As shown in Fig. 9.30, the cells were loaded with dummy crystals that simulate the mass and different gravity vectors have been investigated. The mechanical tests performed on the modular structure provided basic input data to a Finite Element Analysis of the complete support structure.

9.3.10.6 Alveolar module structure finite element analysis

A detailed Finite Element Analysis was performed on the alveolar structure using material properties form data-sheet. The analysis predictions have been compared with the outcome of the load test on Proto2 and the model tuned to best fit the real behaviour. This detailed model, shown in Fig. 9.31, has been used as reference to to validate the Global Finite element model of the whole EMC.

9.3.10.7 Support shell structure design

The shell, shown in Fig. 9.32, consists of the outer cone and front cone as one single solid body in CFRP. The inner cone, where material budget does not pose too stringent limits is a metallic shell. Back plate is the same as BaBar. The volume is defined by the line AB, AD, CD while A'B' and A'D' are construction lines resulting from technical choice.

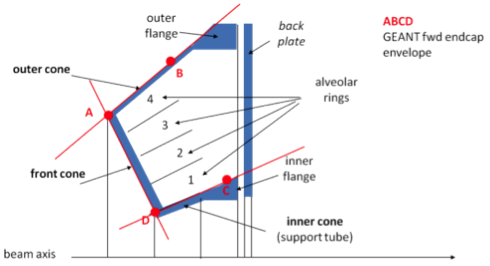

Figure 9.32: Support shell structure

The outer cone end is reinforced by a metallic ring for easy connection with the back plate. The back plate provides the EMC interface with the SuperB bearing points (position reference and transmission of loads). The alveolar array is cantilevered from the shell front cone as detailed in Fig. 9.33.

This configuration provides a logical construction and assembly sequence, in particular an easier and almost reversible access to the most delicate part of the detector, its crystals and photodiodes. There is no connection between the alveolar array and the inner and outer cone inner faces. A 1mm gap is introduced for the free elastic deformations of the alveolar array and of the shell. The front cone is connected to the inner cone by gluing secured by screws.

Support Shell unit production and materials

The outer cone is a massive CFRP (6 to 10mm) while the front cone is either a massive CFRP or a sandwich plate 20mm thick. For the production the mould is at the inner face of the outer-front cone in order to have high dimensional accuracy at the interface with the

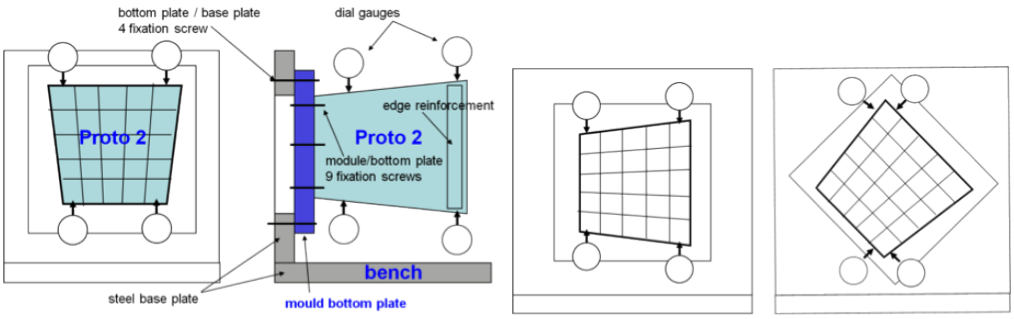

Figure 9.30: alveolar module test setup

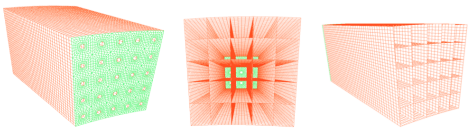

Figure 9.31: Alveolar module finite element model

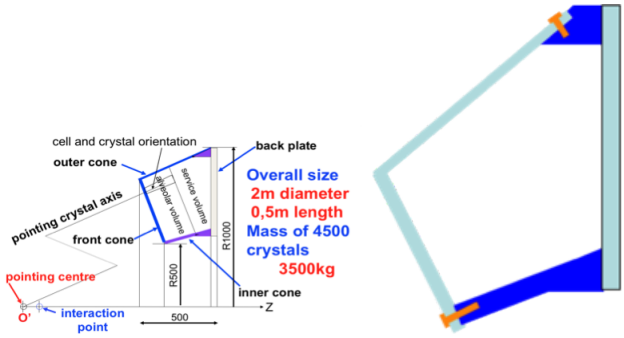

Figure 9.33: Suppert shell assembly

crystals modules, while a vacuum bag is at the opposite side; the parietal aluminum wedge is embedded in the structure The inner cone is a precise CNC machined massive Al 7075 piece with a thickness of 20mm.

9.3.10.8 Global structure finite element analysis

To the front conical plate are connected 180 alveolar modules (of 5 x 5 cells) of four different types, displayed in four concentric rings. Because of the circular configuration each module is in a different loading case. The resulting FE model of the complete distribution of alveolar modules supported by the shell structure would result in a large size, . An alternative parallel solution was followed to reduce the alveolar module to its main useful parameters (superelements) that do not contain all the geometrical detail but that closely characterize the mechanical behavior of the alveola. The input mechanical properties used for the superelements come from the mechanical tests performed on the Proto2.

9.3.11 Performance in simulations[SG]

9.3.11.1 Resolution studies

Can include comparison with *BABAR* forward calorimeter

9.3.11.2 Background studies

9.3.12 Tests on Beam[CC]

9.3.12.1 Description of apparatus

Two tests beam have been performed with a prototype LYSO matrix, one at CERN in October 2010 and one at the Beam Test Facility (BTF) in Frascati in May 2011. The prototype matrix is composed by 25 LYSO crystals of pyramidal shape with dimensions 2.3cm×2.3cm×22cm inserted in a support structure assembled by the RIBA company (Faenza, Italy) described in detail in Sec. 9.3.10. To improve light output uniformity, each crystal presents a black band of 15mm at the end of its smallest face and the area of the face not covered by the APD (or PiN) is painted with a reflective white painting. The mechanics is composed of glass fiber, covered with copper foils $35\mu m$ thick. Between one cell and the other there is a nominal thickness of 200 μm, while the external side has a thickness of 135 μm. Fig.9.3.12.1 shows a picture of the Test Beam structure with inserted one raw of crystals. Of

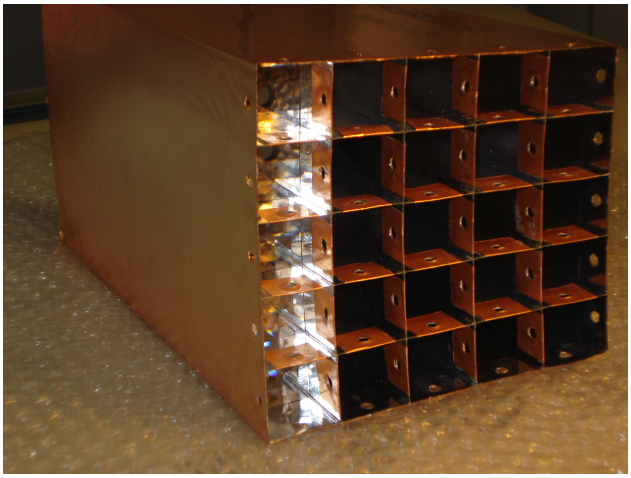

Figure 9.34: Picture of the Test Beam mechanical structure with one raw of LYSO crystals.

the crystals, 20 are read out with an Avalanche Photodiode (APD) in both Test Beams while the remaining 5 are read out with PiN Diodes at the CERN Test Beam and with APDs at the BTF. As shown in Fig. 9.35, the readout chain

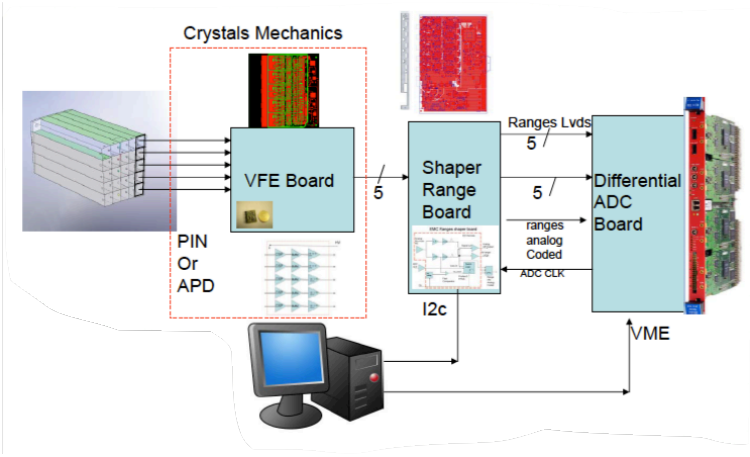

Figure 9.35: Schematic view of the electronic chain for the forward EMC.

Figure 9.36: Schematic view of the test beam setup used at CERN.

is composed of: a front end board (VFE) that contains a Charge Shaper Preamplifier (CSP); Shaper Range Board which completes the attenuation, already applied in the VFE board, and then divides them according to the different energy range. Two different ranges are foreseen in the treatment of the signals, for energies lower than 200 MeV and for energies greater than 200 MeV, although in the test beams the amplifications have been adjusted to use only one range; a 12 bits Caen ADC to process the signals and digitize the analogue outputs. Two different configurations have been used at CERN for the power supply of the APD's, one called High Gain with voltage APD at 380V and one called Low Gain with a voltage of 308V applied.

MISSING TRIGGER

9.3.12.2 Description of the beams

The Beam Test at CERN has been performed at the T10 beam line in the East Area. The beam is mainly composed of electrons, muons and pions created by the scattering of protons into aluminum and tungsten target. The composition of the beam is highly dependent on the energy and for electrons it ranges from 60% at 1 GeV to 1% at 6 GeV. The maximum energy reachable at this beam line is 7 GeV with a nominal momentum spread $\Delta p/p \simeq 1\%$. The distance between the end of the beam line and the matrix is about 15 m. The event rate is of the order of 1 Hz.
Fig.9.36 shows the experimental setup used at CERN, it is composed of a Cherenkov detector already present in the CERN beam line, two scintillators (finger counters) $2\times2\text{cm}^2$, the box containing the matrix and the VFE boards. The Cherenkov detector plus the two scintillators of the fingers act as trigger. The Cherenkov detector allows the separation between electrons and

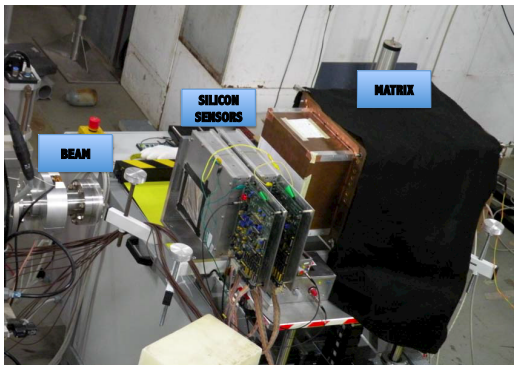

Figure 9.38: Schematic view of the test beam setup used at the BTF in Frascati.

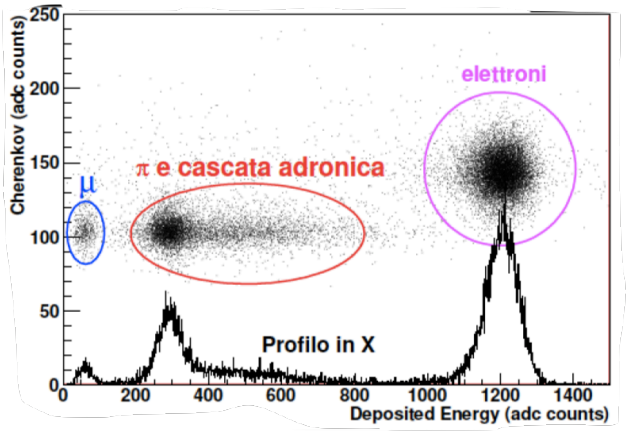

Figure 9.37: Distribution of the signal measured in the Cherenkov detector as function of the total energy deposited in the calorimeter, at 1 GeV.

pions as shown in Fig.9.37 . The same detector has also been used to select Minimum Ionising Particles (MIP) used for the calibration.

The Beam Test Facility in Frascati is part of the ΦFactory, DaΦne. It is composed of a linear accelerator LINAC, one spectrometer and two circular accelerators of electrons and positrons at 510 MeV. The LINAC is the same which supplies the test beam line at the BTF. The pulsed beam of the LINAC circulate electrons up to 800 MeV at a maximum current of 550 mA/pulsation and positrons at a maximum energy of 550 MeV with a current of 100 mA/pulsation. The typical duration of a pulsation is 10 ns, with a frequency of 50 Hz. A bending magnet select electrons of a given momentum, a line of about 12m contains quadrupoles for the uniformation of the beam and a system of slits allow to change the flux of arriving particles. The beam energy spread is 1% at 500 MeV. The setup for the beam test of the matrix at the BTF is shown in Fig.9.38. The setup shows the end of the electron beam line, four planes of silicon strip detector (two measurements in x and two measurements in y) and the box containing the matrix with the crystals and the VFE boards. As mentioned before, at the BTF all the crystals are equipped with APD's, and it should be mentioned that the gain of the VFE has changed with respect to CERN from 0.5 to 1, while an amplification factor has been introduced. To control the position of the beam with respect to the matrix a detector of 16 x 16 scintillating fibers of 3mm each has been used. The trigger is performed by the LINAC radiofrequency (25 Hz), and does not make any use of scintillators.

Since the beam energy spread of the CERN facility proved to be significantly larger than the specifications, based on the performances of the detector at the BTF, we will use the CERN TB data only to study the linearity at high energy, while resolution studies will be performed exclusively on the BTF data.

9.3.12.3 Description of data and calibration

For each triggered event, the output of the readout are the waveforms of the 25 channels, each constituted by 384 samples. The signal amplitude in each channel is defined as the maximum of the waveform, extracted from a guassian fit to the sampling distribution, subtracted of a pedestal. For each crystal, the pedestal is calculated averaging the first 60 samples on a reference run. The pedestal-subtracted amplitude is considered to be the measurement of an energy deposit if it is above a threshold chosen to be three times the noise fluctuation, whose value is determined from a run taken with random triggers where no signal is present.

After calibration, the energy released in the whole matrix, the so-called cluster energy, estimate of the energy of the electron that initiated the shower, was estimated by summing all the energy deposits in all crystals.

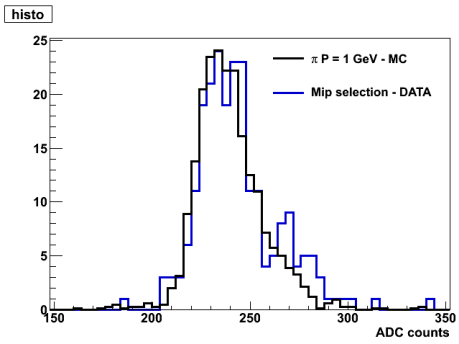

Figure 9.39: Comparison between data and MC of the energy deposited in the MIPs sample. The hypothesis that after the selection the beam is dominated by pions is made.

At the CERN test beam hadrons traversing the crystals horizontally were selected as Minimum Ionizing Particles (MIPs) by requiring no significant signal in the other crystals and a signal consistent with an hadron in the Cherenkov detector. Profiting from the fact that MIPs release a constant amount of energy regardless of their energy, the amplitude spectra of each crystal was fitted to extract the most likely value. After determining on the simulation the expected released energy in each crystal (Fig 9.40) , the corresponding calibration constants could be extracted.

At the BTF test beam, where no hadrons were available, the relative intercalibration constants were obtained on the electron sample itself. The relative cluster energy resolution was minimized by floating a constant in front of each crystal a part from the central one. The overall energy scale was then determined from the knowledge of the beam energy. This procedure was applied on a small fraction of the runs where the electrons were approximately 500 MeV (the highest energy reached in the tests) and the corresponding constants used in all other runs. This intercalibration was also cross-checked by means of cosmic-ray data obtained with an ad-hoc trigger made of two plastic scintillator pads positioned above and below the crystal matrix(see Fig. **??**). The channels where there is a significant difference are those where the electron data see very little energy because they are far from the center of the matrix. In such cases, that have little impact on the resolution studies since they contribute little to the total energy measurement, the MIPs intercalibrations are used.

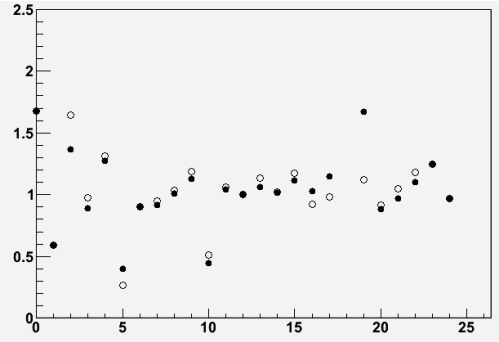

Figure 9.40: Comparison between electron and MIPs calibration at the BTF test beam as a function of the crystal number. Calibration constants are referred to crystal 12 that is therefore by definition equal to unity.

9.3.12.4 Electronics noise measurements

The first information we could extract from the data are the characteristics of the electronic noise. From the signal distribution in a random trigger run at the BTF we estimated (Fig. 9.41) that a part from two channels, the noise is on average 2ADC counts. After applying the calibration, this noise corresponds to approximately 0.4MeV. To understand if there were resonant components, the noise of each crystal i was analyzed in the Fourier space, by estimating its power spectrum from waveforms acquired with a random trigger:

$$\mathrm{PS}_i(\omega_k) =< n_i(\omega_k) n_i^*(\omega_k) > . \qquad (9.3)$$

The estimated power spectrum of a representative channel is shown in Fig. 9.41, where it can be seen that the dominant source of noise is in the range 0-8 MHz, which corresponds to the frequency bandwidth of the shaper. Sources of noise occurring after the shaper give a negligible contribution, while those occurring before are filtered according to the shaper transfer function and dominate.

We investigated the presence of a possible correlation between the noise observed on different crystals. The correlation can be in principle present, because the APDs in the matrix are biased by a unique power supply, and each Front End board serves 5 crystals.

The covariance between crystals i and j has been estimated as

$$\mathrm{COV}_{ij}(\omega_k) =< n_i(\omega_k) n_j^*(\omega_k) > \qquad (9.4)$$

The magnitude of an element of these matrices is the covariance between two crystals as usually intended in the real domain, while the phase is the relative time delay between them. As a consequence the correlation is also a complex quantity, which is defined as:

$$\rho_{ij}(\omega_k) = \frac{\mathrm{COV}_{ij}(\omega_k)}{\sqrt{\mathrm{PS}_i(\omega_k)\mathrm{PS}_j(\omega_k)}} . \qquad (9.5)$$

This study concluded that the noise correlation is negligible, and that each crystal has an independent noise source. The two crystals with the highest correlation below 8 MHz were number 2 and 10, and the corresponding correlation as a function of the frequency is shown in Fig. 9.42. It can be seen that the correlation is, on average, very small in the region of interest.

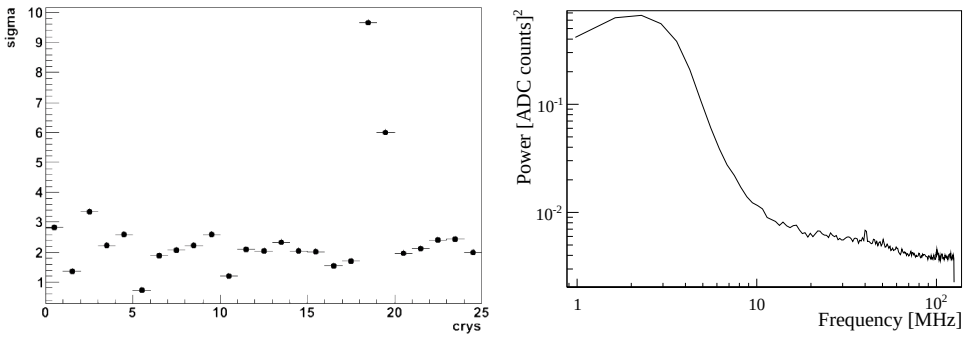

Figure 9.41: Left: Noise RMS for each channel of the BTF test beam. Right: power spectrum of a representative channel.

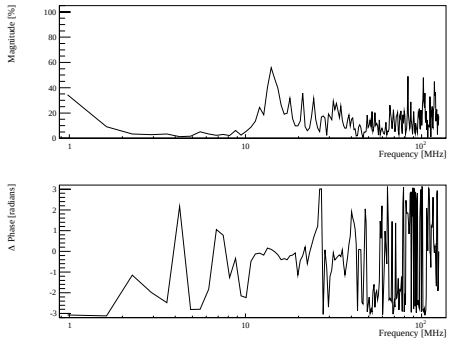

Figure 9.42: Correlation between crystals 2 and 10 as a function of the frequency. The phase takes random values when the magnitude is zero, when this happens its value should not be considered.

9.3.12.5 Temperature corrections

A temperature dependence of several percent per degree is expected both in the light yield of the LYSO crystals and in the gain of the APDs. At the CERN test beam the position of the MIP peak as a function of the temperature measured by sensors places on the rear of the crystals has been used to extract the temperature correction (Fig. 9.43) : $E_{corr} = E_{raw}/(1 - p_0 * (T - T_0))$ where $p_0 = 2.8 \pm 0.2 \times 10^{-3}$ and $T_0 = 34$K. The same figure shows also the effect of the correction.

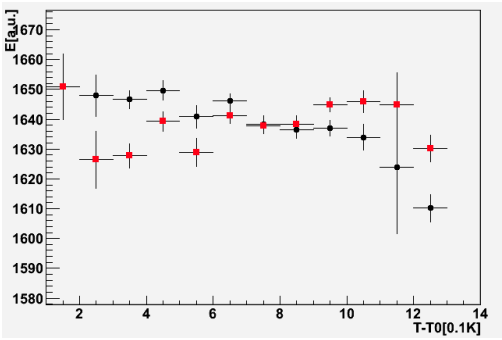

Figure 9.43: Dependence of the measured energy on the temperature before (black dots) and after (red squares) correction.

This correction proved irrelevant at the BTF test beam where the temperature was controlled to better than 0.2^oC

9.3.12.6 Algorithms and results

9.3.13 Alternatives

9.3.13.1 Pure CsI

Description

Performance, tests

Mechanical changes

Electronics changes

9.3.13.2 BGO

Description

Performance, tests

Mechanical changes

Electronics changes

9.3.13.3 Hybrid Alternative

Table 9.3.13.3 is a comparison of the volume and total cost of the scintillating crystals required for the forward endcap in several different configurations. The baseline design, employing LYSO crystals, contemplates complete replacement of the existing mechanical structure. A new carbon fiber aveolar and associated structure to mount the crystals on the doors of the magnet is estimated in the Super$B$ TDR to cost euro X.Y. The total cost of the endcap is the sum of the crystal production and preparation costs, the photosensor readout and associated electronics, the mechanical structure, associated cooling and electronic services and the calibration system. Thus the crystal cost is only one component, *albeit* the largest, of the system.

There are nine rings of for crystals in the existing *BABAR* CsI(Tl) endcap structure. Complete replacement of the CsI(Tl) requires 3600 LYSO or BGO crystals or 900 pure CsI crystals. Table 9.3.13.3 shows the volume of crystals required for complete replacement and the estimated costs for these crystals, but does not include the other mechanical or readout costs listed above.

The table also lists three hybrid options, in which a number of the outer CsI(Tl) rings of the endcap are retained (since they are approximately at the same distance from the interaction region as are the forward barrel crystals) and the inner rings are replaced by LYSO crystals. The retention of the existing *BABAR* mechanics is intrinsic to this option, providing a substantial additional savings. As the Moliére radius of LYSO is one half that of CsI(Tl), four LYSO crystals can be placed into one CsI(Tl) compartment. If three CsI(Tl) rings are retained, the required volume of LYSO is reduced by 40%. Including the savings in mechanics, this represents a factor of two reduction in the cost of the endcap. The volumes for replacement of four and five of the nine rings are also included in the table.

Option	Number of New Crystals	New Crystal Volume (cc)	Cos
LYSO full (baseline)	3600	330559	2
3 CsI(Tl) + 6 LYSO	2160	195590	2
4 CsI(Tl) + 5 LYSO	1760	156412	2
5 CsI(Tl) + 4 LYSO	1360	118672	2
Pure CsI	900	680140	
BGO	3600	330000	

Table 9.5: Comparison of crystal volume and crystal costs for several forward endcap configuration options.

9.3.13.4 Comparison with baseline

Includes a brief discussion of other, discarded, options

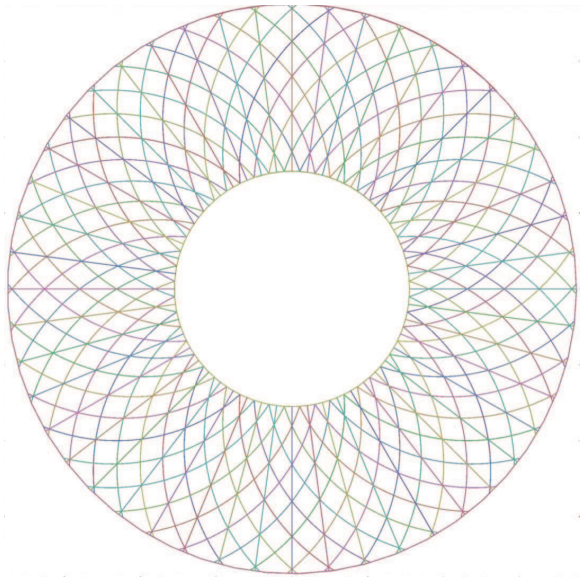

Figure 9.44: The backward EMC, showing the scintillator strip geometry for pattern recognition.

9.4 Backward Calorimeter

The backward electromagnetic calorimeter for Super$B$ is a new device with the principal intent of improving hermeticity of the detector at modest cost. Excellent energy resolution is not a requirement, since there is significant material from the drift chamber in front of it. Thus a high quality crystal calorimeter is not planned for the backward region. The proposed device is based on a multi-layer lead-scintillator sampling calorimeter with longitudinal segmentation providing capability for π/e separation. The design is derived from the analog hadron calorimeter for the ILC.

The backward calorimeter is located behind the drift chamber starting at z= -1320 mm (see Figure **??**) allowing room for the drift chamber front end electronics. The inner radius is 310 mm, the outer radius is 750 mm and its total thickness is less than 180 mm covering $12X_0$. It is constructed from a sandwich of 2.8 mm Pb plates alternating with 3 mm plastic scintillator strips (*e.g.*, BC-404 or BC-408). The scintillation light of each strip is collected by a wavelength-shifting fiber (WLS) coupled to a photodetector located at the outer radius. The scintillator strips come in three different geometries, right-handed logarithmic spirals, left-handed logarithmic spirals and radial wedges. This pattern alternates eight times. Each layer contains 48 strips producing a total of 1152 readout channels. The strip geometry is illustrated in Fig. 9.44

The WLS fibers, Y11 fibers from Kuraray, are embedded in grooves milled into the center of the scintillator strips. Each fiber is read out at the outer radius with a $1 \times 1\,\mathrm{mm}^2$ multi-pixel photon counter (SiPM/MPPC) [**?**]. A mirror is glued to each fiber at the inner radius to maximize light collection. The SPIROC (SiPM Integrated Read-Out Chip) integrated circuit (IC) [**?**] developed for the ILC is used to amplify and digitize the SiPM/MPPC signals, providing both TDC (100 ps) and ADC (12 bit) capability. Each ASIC contains 36 channels. Since these ASICs were developed for SiPM readout, where the intrinsic gain is much higher, an additional preamplifier is coupled to the SiPM/MPPCs. This has the advantage to place the SPIROC ASICs at a convenient place in the detector without introducing additional noise.

9.4.1 Requirements

The main goal of the backward endcap EMC is to record any charged or neutral particle. This information is important for analyses that study the recoil of a B meson fully reconstructed in hadronic or semileptonic to reduce backgrounds. In fact the detector can be used as veto device to reject events in which neutral energy, not associated to the reconstructed B's, is recorded in the backward EMC. More detailed studies on the backward device may also lead to the decision of using it in the reconstruction process and this may also enhance the reconstruction efficiency, depending on the number of neutrals contained in the B channels of interest. Furthermore, the time-of-flight and energy loss via ionization capability is useful to perform particle identification.

9.4.1.1 Energy and angular resolution

Since the backward EMC prototype is still in the construction phase, presently no results on energy resolution and angular resolution exist. However, electromagnetic sampling calorimeter prototypes with plastic scintillator strips and tiles have been tested in test beams within the CALICE collaboration [**?**]. The energy resolution for the stochastic term is $15\%\sqrt{E}$ and for the constant term is around 1%. For the CALICE analog hadron calorimeter which has a non-optimized geometry for electromagnetic showers, the stochastic term was measured to be around $20\%/\sqrt{E}$. For low photon energies, an additional noise term of ~ 130 MeV$/E$ contributes. Thus, the backward endcap EMC is expected to have a similar performance with a stochastic term of $15 - 20\%/\sqrt{E}$.

The left-handed logarithmic spirals are defined by

$$x(t) = r \exp b \cdot t \cos t - r \tag{9.6}$$

$$y(t) = r \exp b \cdot t \sin t \tag{9.7}$$

$$\tag{9.8}$$

For $r = r_o/2 = 37.5\ cm$ and $b = 0.2$ eight left-handed spiral strips overlap with eight right-handed spiral fibers defining a specific tile-shaped region. The radial strips overlap with five left-handed (right-handed) spiral strips. In the worst case the resolution is $\sigma_r = \sigma_\phi \simeq$ 29 mm in the outer region. This is improved to $\sigma_r = \sigma_\phi \simeq 12$ mm in the inner region.

9.4.1.2 Background rates

Present background simulations indicate that the worst n rate in layer zero of the backward IFR end cap is 3.5 kHz/cm^2. The radiation profile shown in Figure **??** indicates that the worst rates for all energies of 3 kHz/cm^2 occur in the inner most region. In ten years of running this amounts to 6.1×10^9 n/mm^2 in the region near the inner radius. The background rates drop by significantly towards outer radius. At the the location of the photodetector, the rate is reduced by more than a factor of 10. Further simulation studies are needed, since due to the high rate at the inner radius an occupation problem may be present. To deal with this issue one either subtracts a higher average background energy from each strip or divides the strips into two segments at the cost of doubling the number of photodetectors. The former solution will have an effect on the energy resolution since the background energy deposit has a wide distribution. The latter solution is preferable, but is about \$100k more expensive.

9.4.1.3 Radiation hardness

Irradiation of Si detectors causes the dark current to increase linearly with flux Φ:

$$\Delta I = \alpha \Phi V_{eff} G, \tag{9.9}$$

where $\alpha = 6 \times 10^{-17}$ $A/cm V_{eff} \sim 0.004\,\mathrm{mm}^3$, Φ is the flux, V_{eff} is the bias voltage and G is the gain. Since the initial resolution of SiPMs of $\sim 0.15pe$ is much better than that of other Si detectors, radiation effects start at lower fluxes. For example, at a flux $\Phi = 10^{10}/cm^2$ the individual single pe signals are smeared out. The MIP peak is still visible at $\Phi \sim 10^{11} n/cm^2$. The number of observed hot spots and the noise rate increase after irradiation of $3 \times 10^9 n/cm^2$. No significant changes on the cross talk probability and no significant change on the saturation curves are observed. The main effect is an increase in noise after exposure to high n dose. Hamamatsu has produced news SiPM/MPPCs with 20 $\mu m \times 20$ μm and 15 $\mu m \times 15$ μm, which have lower detection efficiency due to more boundaries and thus need a higher bias voltage to compensate for losses. Figure **??** shows the detection efficiency as a function of bias voltage for 15 $\mu m \times 15$ μm detectors before and after irradiation. For the new detectors, signal/noise and the equivalent noise charge look fine after irradiation. According to Eugenios study the backward endcap EMC will record 10^9 $n\,\mathrm{mm}^2$ after 10 years operation. Thus, if the 25 $\mu m \times 25$ μm pixel SiPM/MPPC show a problem we switch to one of the new SiPM/MPPCs with smaller pixel size.

9.4.1.4 Solid angle, transition to barrel

The backward endcap EMC covers a polar angle region from to .

9.4.2 Mechanical design

The 3 mm thick scintillator strips are cut individually from a scintillator plate. Thus, the plate size and the cutting procedure need to be carefully thought through to minimize the amount of waste. For the spiral strips the least waste and fastest production is obtained by fabricating a mould. However, this approach may be too expensive since the total number of spiral strips is rather small. The preferred scintillator material is BC 404 from St Gobain, since it has the smallest decay time for TOF capability and its emission spectrum is reasonably matched to the Y11 absorption spectrum. The strip width is 38 mm at the inner edge increasing to 98 mm at the outer edge. The sides are painted with a white diffuse reflector. Front and back faces are covered with reflectors sheets (3M, Tyvec). To restore uniformity, a pattern of black dots is printed onto the white reflector sheets.

In the center of each strip, a 1.1 mm deep groove is milled into which the 1 mm thick Y11 WLS fiber is inserted. At the outer edge of the strip, the groove is cut a 0.4 mm deeper so that the SiPM/SiPM/MPPC fully covers the fiber. The SiPM/MPPC is housed in a small precisely cut pocket. Especially fabricated fixtures out of Teflon or Nylon will hold a strip. The fiber groove at the outer edge is closed with a plug at the position of the photodetector. The Y11 fiber is pressed against the plug and held with a drop of glue. After removing the plug the SiPM/MPPC is inserted and is glued onto the Y11 fiber to match refractive indices. A mirror is placed at the other end of the fiber to detect the light that moves away from the photodetector. So tolerances in the length of the Y11 fiber are picked up at the mirror end. The strip layout is shown in Figure **??**.

To hold the strips in each layer in place 1.5 mm deep and 1 mm wide grooves are cut into the lead plates. The shape of groove matches that of the strip. A 3 mm thick and 1 m wide and 550 mm long plastic strip is inserted into the groove and is glued. This structure is strong enough to hold the scintillator strips in place. The calorimeter can be rotated by 90°. This is needed for operation with cosmic muons that yield a MIP calibration and allows for testing the calorimeter before installing it into the SuperB detector.

The entire calorimeter just weighs about 1300 Kg. An Al frame with a strong back will hold the EMC backward EC layers. It has several advantages (performance and costs) to build the backward endcap as a single unit. This requires the endcap to slide back on the beam pipe supported on the tunnel walls. It needs to be fixed at the tunnel and is rolled in. Since the inner radius is 31 cm, there is sufficient clearance for pumps and other beam elements. The design of this capability requires a detailed drawing of the beam pipe and the position and size of machine elements.

It is possible, however, to build the backward endcap in two halves with a vertical split. The impact of such a design is that ten strips per layer have to be cut into two segments, where the inner segments have to be read out at the inner radius. This increases the number of channels by 240, requiring 240 additional SiPM/MPPCs, seven extra SPIROC boards and four extra calibration boards. This layout

Table 9.6: Properties of Hamamatsu MPPCs

MPPC type	# cells $1/mm^2$	C [pF]	R_{cell} [$k\Omega$]	C_{cell} [fF]	$\tau = R_c \times C_c$ [ns]	$V_{break\ down}$ [V] at T=23 C	V_op [V] at T=23 C	Gain [10^5]
15 μm	4489	30	1690	6.75	11.4	72.75	76.4	2.0
20 μm	2500	31	305	12.4	3.8	73.05	75	2.0
25 μm	1600	32	301	20	6.0	72.95	74.75	2.75
50 μm	400	36	141	90	12.7	69.6	70.75	7.5

will deteriorate the performance near the vertical boundary. The effect needs to be studied in simulations. This certainly adds extra costs at the order of $\sim 20\%$.

9.4.2.1 Calorimeter construction

9.4.2.2 Support and services

·¿¿¿

Each SPIROC board has !36*6 cables one multiplexed output (USB) to DAQ a low voltage input for +5.5 V and -7.5V a high voltage input 70V an electronic calibration input an analog output Each calibration board has !16*8 cables low voltage for LED 7V operating voltage 6 PIN diode output 4 thermocouples per layer !24*4 cables Total number of cables 108+128+96=332 cables ! area: 100*0.3 cm2

9.4.3 SiPM/MPPC readout

The photodetectors are SiPM/MPPCs from Hamamatsu (type) with a sensitive area of $1\ mm \times 1\ mm$ holding 1600 pixels with a size of $25\ \mu m \times 25\ \mu m$. These detectors are avalanche photodiodes operated in the Geiger mode with a bias voltage slightly above the breakdown corresponding to $50 - 70\ V$ providing a gain of a few 10^5. They are insensitive to magnetic fields. Each pixel typically has a quenching resistor of a few $M\Omega$ so they recover within 100 ns. The efficiency is of the order of $10 - 15\%$. Since the SiPM/MPPCs record single photoelectrons, they are auto-calibrating. They are non-linear requiring non-linearity corrections for higher energies. The dynamic range is determined by the number of pixels. The properties of SiPM/MPPCs are listed in Table 9.6.

A concern with SiPM/MPPCs is radiation hardness. Degradation in performance is observed in studies performed for the Super$B$ IFR, beginning at integrated doses of order 10^8 1-MeV-equivalent neutrons/ cm^2 [?]. This needs to be studied further, and possibly mitigated with shielding. Another alternative is look into a different photodetector. Recently, Hamamatsu has produced SiPM/MPPCs with pixel sizes of $20\ \mu m \times 20\ \mu m$ and $15\ \mu m \times 15\ \mu m$ (see Table ??). A CMS study shows that the performance of these new photodetector deteriorates only slightly after an irradiation of $10^{13} n/cm^2$.

9.4.4 Electronics

The signal of the SiPM/MPPC is first amplified with a charge-sensitive preamplifier then fed into the auto-triggered, bi-gain SPIROC ASIC. The SPIROC board has 36 channels. Each channel has a variable-gain charge preamplifier, variable shaper and a 12-bit Wilkinson ADC. It allows to measure the charge Q from one photoelectron (pe) to 2000 pe and the time t with a 100ps accurate TDC. A high-level state machine is integrated to manage all these tasks automatically and control the data transfer to the DAQ. The SPIROC ASIC was designed to supply the high voltage for the SiPM/MPPC. Using a DAC, individual high voltages within $\pm 5\ V$ can be supplied to each photodetector.

The SPIROC ASIC gives Gaussian signals with no tails, shows excellent linearity and low noise. 32 ASIC readout boards are needed to read out the entire endcap. The boards are mounted in two layers behind the endcap. The first layer hold 20 boards and the second layer the remaining 12 boards. Each board connects to 36 SiPM/MPPCs via a ribbon cable that were designed for ILC at a luminosity of $\mathcal{L} = 10^{34} cm^{-2} s^{-1}$.

9.4.5 Calibration

An LED-based calibration system with fixed LED intensities is used to monitor the stability of strip-fiber-SiPM/MPPC system between MIP calibrations, to perform gain calibrations, determine intercalibration constants, and to measure the SiPM/MPPC response functions. This is necessary since the SiPM/MPPCs have a temperature and voltage dependence of the gain

$$\frac{dG}{dT} \sim -1.7\%/K \tag{9.10}$$

$$\frac{dG}{dV} \sim 2.5\%/0.1V \tag{9.11}$$

The temperature and voltage dependence of measuring the charge of the scintillation signal is

$$\frac{dQ}{dT} \sim -4.5\%/K \tag{9.12}$$

$$\frac{dQ}{dV} \sim 7\%/0.1V \tag{9.13}$$

Using the design of the calibration system for the analog hadron calorimeter prototype, the calibration system is based on an UV LED that couples to 19 clear fibers, of which 18 fibers transfer light to 18 strips and one fiber is readout by a PIN photodiode to monitor the LED light. Twelve LEDs are mounted on each calibration board. The fibers are routed a the outer edge. They are inserted into a hole in the strip. Thermocouples distributed throughout the outer edge of the endsap measure the temperature which is recorded regularly together with the voltage by a slow control system. After PIN diode correction the stability of LED system is $< 1\%$. For the analog hadron calorimeter a study is performed in which one fiber serves several tiles by providing cuts at appropriate postions so that the light is extracted there. If this work it would reduce the number of fibers and calibration boards considerably.

Since the CMB boards are too big to be mounted at the outer radius of the endcap, new boards need to be produced. Using the same concept half-size boards with six LEDs are produced. If each LED couples to 19 fibers, 11 boards are sufficient.They can be mounted in

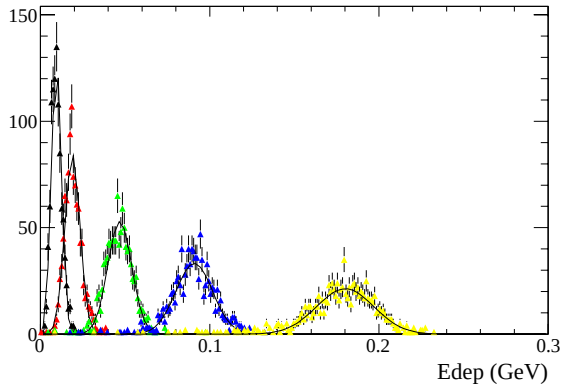

Figure 9.45: Energy depositions in the scintillators of the backward EMC from mono-energetic photons of various energies generated in front of the EMC. See text.

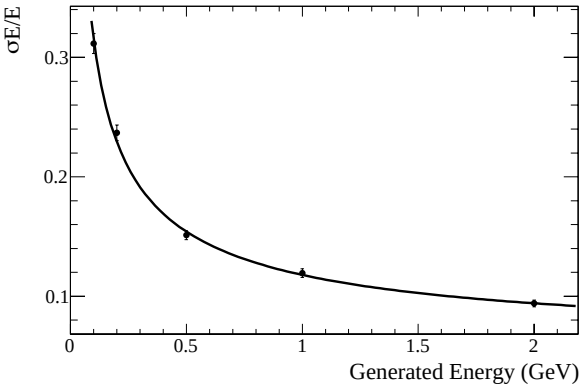

Figure 9.46: The backward EMC energy resolutions, σ_E/E, where σ_E and E are the Gaussian width and mean in Fig. 9.45, as a function of generated photon energy.

two rings around the endcap. To avoid to small bending radii LEDs from the right ring supply strips to the left and LEDs from the left ring supply strips to the right. So in total, 64 LEDs and 64 PIN diodes are needed.

9.4.6 Backward simulation

Currently there only exists a simple backward EMC model in GEANT4 simulation. The scintillator and the lead are modeled. Each layer is modeled with a complete disc without physical segmentations in r-ϕ. The supporting structure, fibers, electronics, and cables are not modeled yet.

A GEANT4 simulation is performed to study the energy resolution. We simplify the conditions by ignoring the rest of the detector and shoot mono-energetic photons perpendicular to the face of the disc. All energy deposited in the scintillator is collected. No clustering algorithm is performed. Figure 9.45 shows the energy deposition for five different energy photons, 100, 200, 500, 1000, and 2000 MeV. On average approximately 9.5% of the photon energy is deposited in the scintillator for 100 MeV photons. This percentage drops to 9.0% for 2 GeV photons.

The energy resolution dependence on generated energy is shown in Fig. 9.46. It can be fitted with the function $\sigma_E/E = \frac{10\%}{E(\mathrm{GeV})^{0.485}} \oplus 6\%$.

In the fast simulation, the model does not separate lead from scintillator. It uses an artificial material that approximates the overall density, radiation length, interaction length and Moliere radius of the mixture of lead and plastic. The volume is divided into eight rings, each of which is divided into 60 segments. We do not model the logarithmic spirals and lead-scintillator layers to avoid complicated cluster reconstruction and longitudinal shower energy distribution modeling. The energy resolution used in the fast simulation is $\sigma_E/E = \frac{14\%}{\sqrt{E(\mathrm{GeV})}} \oplus 3\%$.

9.4.7 Impact on physics results

Fast simulation studies have been performed to investigate the performance gain achieved by the addition of the backward calorimeter. The channels chosen to evaluate the impact of this device are $B \to \tau\nu$ and $B \to K^{(*)}\nu\bar{\nu}$, since they are both benchmark channels for the Super B physics program, and two crucial ingredients for their measurement are the neutral energy reconstruction and the detector hermeticity.

The study of the leptonic decay $B \to \tau\nu$ is of particular interest as a test of the Standard Model (SM) and a probe for New Physics. The presence of a charged Higgs boson (in *e.g.*, a Two Higgs Doublet Model) as a decay mediator could significantly modify the branching ratio with respect to the SM value, depending on the Higgs mass and couplings [1]. A complementary search for physics beyond the SM can be performed using $B \to K^{(*)}\nu\bar{\nu}$ decays [2]. Being mediated by a flavour changing neutral current, these processes are prohibited at tree level in the SM and the higher order diagrams may receive contribution from non-standard mechanism. Moreover, new sources of missing energy may replace the neutrinos in the final state.

The aforementioned decays are challenging to identify, as the final state contains more than one neutrino and can only be partially reconstructed. Signal events are selected using a recoil technique, where the signal B-meson (B_{sig}) is identified as the recoiling system against the other B in the event (B_{reco}). The B_{reco} are reconstructed either in hadronic or semileptonic decay modes, similar to the ones described in Ref. [3]. The rest of the event is assigned to the $B \to \tau\nu$ candidate if it is compatible with one of the following decay modes of the τ lepton: $\mu\nu_\mu\nu_\tau$, $e\nu_e\nu_\tau$, $\pi\nu_\tau$, $\pi\pi^0\nu_\tau$, $\pi\pi^0\pi^0\nu_\tau$, $\pi\pi\pi\nu_\tau$, $\pi\pi\pi\pi^0\nu_\tau$. These final states cover about 95% of the total τ width, and have one (1-prong) or three (3-prong) charged particles, with the possible addition of a π^0. Candidates for the $B \to K^{(*)}\nu\bar{\nu}$ sample should be compatible with one of the following final states: $K^{*+} \to K_S(\pi^+\pi^-)\pi^+$, $K^+\pi^0$, $K^{*0} \to K^+\pi^-$, K^+, $K_S \to \pi^+\pi^-$ (semileptonic analysis only). In the analyses with a $K^{(*)}$ in the final state further selection criteria are applied, using kinematical quantities related to the goodness of the B_{reco} and $K^{(*)}$ reconstruction and event shape variables testing the energy balancing in the event and the presence of missing energy due to the neutrinos in the final state. This stage of the analyses is very similar to the ones in Ref. [3] for the hadronic and semileptonic $B \to K^*\nu\bar{\nu}$, and the one in Refs. [4] for the $B \to K\nu\bar{\nu}$ semileptonic analysis.

Besides the B_{reco} and B_{sig} selection, the background is mainly rejected using the total neutral energy in the detector of particles not associated with either B-meson, E_{extra}. Signal events peak at low E_{extra}, while background events, which contain additional sources of neutral clusters, tend to be distributed at higher values. The discriminating power of this variables obviously increases with the calorimeter coverage. For this analyses, two different quantity realted to the neutral energy deposit have been calculated: E^{extra}_{brrfwd} and E^{extra}_{bwd} computed using extra-photons reconstructed in both the Barrel and Forward regions and in the Backward region only, respectively. Since E^{extra}_{brrfwd} is uncorrelated to E^{extra}_{bwd}, in order to retain more statistics

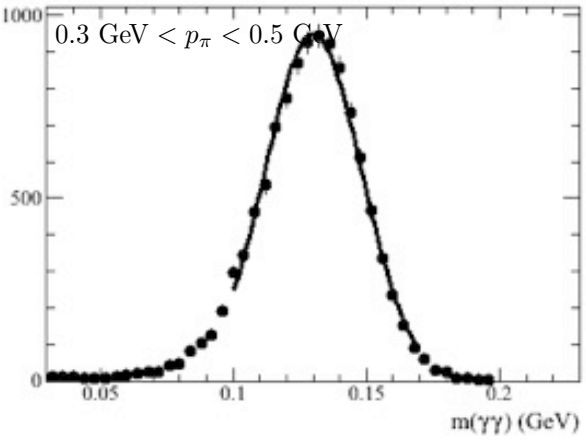

Figure 9.49: Invariant mass resolution of $\pi^0 \to \gamma\gamma$ where one photon is detected at the backward EMC.

the former is not used in the selection while the latter is exploited when studying the backward EMC impact. Its performances are evaluated using the statistical precision, $S/\sqrt{S+B}$, where S denotes the number of signal events surviving the selection criteria, and B the number of background events from a $B\bar{B}$ MC cocktail representing the main analysis background. The impact of the backward EMC is quantified by calculating the variation of the statistical precision with and without applying a veto on the E_{bwd}^{extra} presence. The effect of background events superimposed on the physics event, as described in Sec.XXX, has been incorporated.

The results are summarized in Table 9.7 for the $B \to K^{(*)}\nu\bar{\nu}$ and $B \to \tau\nu$ reactions. For the hadronic $B \to \tau\nu$ channel, the change in the figure of merit depend on the reconstructed τ mode, while in the semileptonic analysis, the different contributions are averaged over all τ final states. The relative gain in $S/\sqrt{S+B}$ is between 3% and 10% depending on the reconstructed signal mode. A 6% improvement on the signal significance has also been observed.

The numbers in Table 9.7 can be translated in precision on physical quantities. An example is given in Figure 9.47, where the expected precisions on the $B \to K^+\nu\bar{\nu}$ and $B \to K^*\nu\bar{\nu}$ branching fractions evaluated as a function of the integrated luminosity are shown. The yellow band represents the theoretical prediction in the SM framework from Ref. [1]. The points with the red band errors are obtained by extrapolating the BaBar experimental results, taking into account the improvement due to the lower boost which results in a higher detector hermeticity. The points with the black band errors are obtained using the same method but considering also the benefits from the usage of the backward EMC as a veto device. For the $B \to K^+\nu\bar{\nu}$ and $B \to K^*\nu\bar{\nu}$ the 3 σ significance for the evidence is reached at 5 ab^{-1} and 51 ab^{-1}, respectively, while adding the backward EMC the needed statistics to have the same sensitivity lowers to 4.5 ab^{-1} and 42 ab^{-1}, respectively.

In addition to acting as a veto device, the backward EMC can also be used to improve the π^0 reconstruction efficiency. The $\gamma\gamma$ invariant mass resolution where one photon isreconstructed in the backward endcap is around 24 MeV for 200 MeV/c π^0 and about 13 MeV at 1 GeV/c (See, e.g., Fig. 9.49).

We evaluate the impact on the B reconstruction efficiency using $B^- \to D^0\pi^-, D^0 \to K^-\pi^+\pi^0$. Events are separated into two groups: the first uses only photons from the barrel and forward endcap, while the second includes photons from the backward EMC with polar angle between $-0.96 < \cos\theta < -0.89$ as well. The π^0

Table 9.7: Relative change in $S/\sqrt{S+B}$ due to the usage of the backward EMC as veto device, on $B \to K^{(*)}\nu\bar{\nu}$ and $B \to \tau\nu$ for semileptonic and hadronic recoil analyses. The first uncertainty is statistical and the second systematic.

channel	Semileptonic	Hadronic
$B \to \tau\nu$	$(6.1 \pm 0.1 - 0.7)\%$	$\simeq 3 - 5\%$
$B \to K^+\nu\bar{\nu}$	$(5.8 \pm 1.0 - 0.6)\%$	-
$B \to K_S\nu\bar{\nu}$	$(6.0 \pm 0.4 - 0.6)\%$	-
$B \to K^{*+}(K^+\pi^0)\nu\bar{\nu}$	$(7.0 \pm 0.2 - 0.7)\%$	$(5.9 \pm 2.5 - 0.5)\%$
$B \to K^{*+}(K_S\pi^+)\nu\bar{\nu}$		$(6.2 \pm 2.1 - 0.5)\%$
$B \to K^{*0}\nu\bar{\nu}$	$(9.1 \pm 0.4 - 0.7)\%$	$(7.3 \pm 1.8 - 0.5)\%$

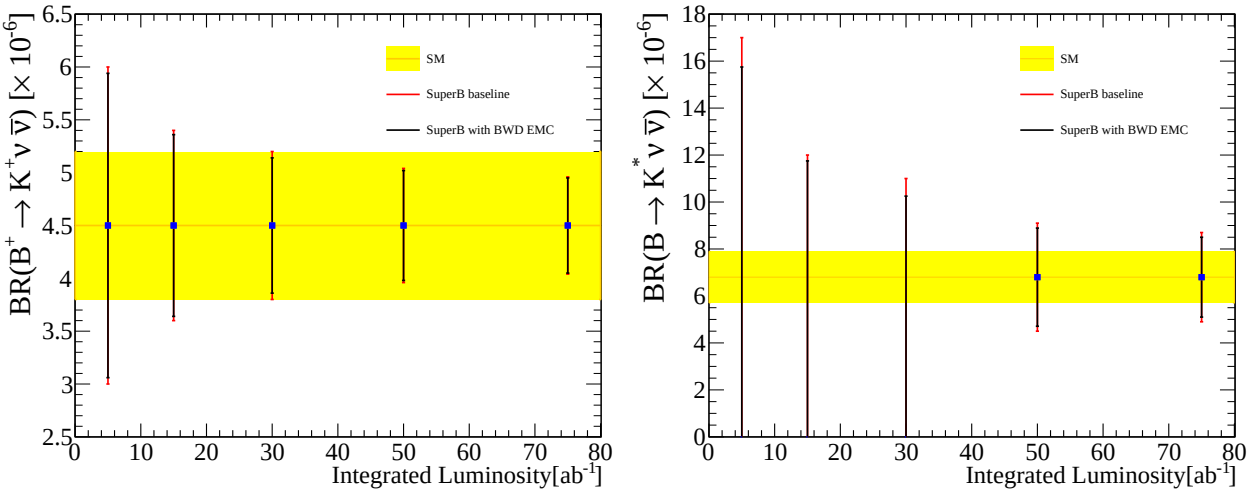

Figure 9.47: Expected precision of the measurements of the branching fractions of (left) $B \to K^+\nu\bar{\nu}$ and (right) $B \to K^*\nu\bar{\nu}$ evaluated as a function of the integrated luminosity. The yellow band represent the theoretical expectation for the SM branching fraction, the black (red) error bars represent the upper limits or the branching ratio measurements with (without) bacward EMC.

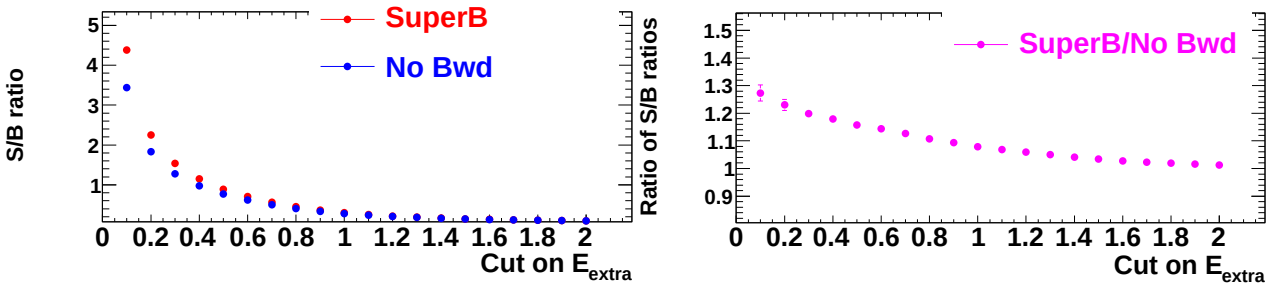

Figure 9.48: Left: Signal-to-background ratio with and without a backward calorimeter, as a function of the E_{extra} selection. Right: Ratio of the S/B ratio with a backward calorimeter to the S/B ratio without a backward calorimeter, as a function of the E_{extra} selection.

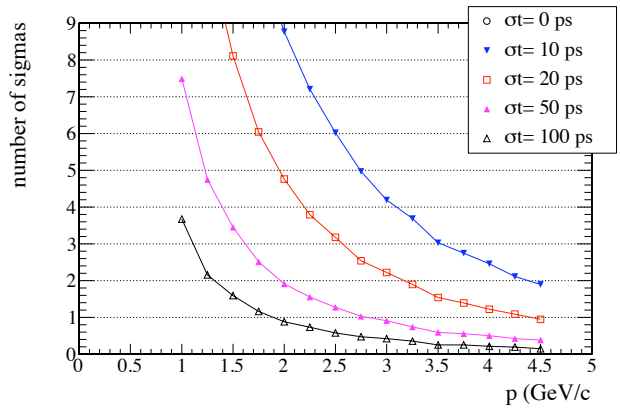

Figure 9.51: Kaon-pion separation versus measured momentum for different timing resolutions in the backward EMC region. The finite separation for perfect timing resolution is because measured momentum is used.

mass window is defined as 120–145 MeV (100–180 MeV) for the first (second) group. We select D^0 within $1.830 < m_{K\pi\pi^0} < 1.880$ GeV, and $-80 < \Delta E < 50$ GeV for B candidates. The $m_{\rm ES}$ distribution is finally fitted to determine the B reconstruction efficiency. We find that including the backward calorimeter, the signal efficiency increasesby nearly 4% in this particular channel (Fig. 9.50).

9.4.8 Impact on particle identification

Charged particles moving in the backward direction typically have lower momentum, and ionization loss and time-of-flight measurements may therefore provide useful particle identification information, *e.g.* for K/π separation.

A preliminary study is performed with fast simulation, generating single kaons or pions pointing towards the backward endcap. The true arrival time at the first layer is smeared with a Gaussian resolution as the measured time. The velocity is calculated from the reconstructed track path length and the measured time K/π separation in terms of σ is extracted using the mean and RMS of the velocity distributions. This procedure includes uncertainties from momentum measurement and path length reconstruction. For example for 100 ps time resolution, Figure 9.53 shows K/π separation in units of standard deviations as a function of momentum. A separation of more than three standard deviations (σ) can be achieved for momenta up to 1 GeV/c and approximately 1.5σ up to 1.5 GeV/c.

Since each layer measures the time distribution, 24 measurements will be averaged. In addition to timing, the ionization is measured in each layer. For MIP-like particles, the average energy loss per layer is $dE_{Pb} = 4.3$ MeV and $dE_{sintillator} = 0.6$ MeV. A 0.5 GeV π is at the ionization minimum, while a 0.5 GeV K is below the minimum. For MIP particles, the ionization loss in the 24 layers is $DeltaE = 117$ MeV. Since the energy loss below the minimum increases with decreasing momenta as $1/\beta^2$, dE/dx measurements in the endcap can be combined with the dE/dx information from the SVT and DCH. Figure **??** shows the ionization curves for e, μ, π, K and p as a function of momentum. A $> 3\ \sigma$ K/π separation is achievable for momenta up to $0.6 - 0.7$ GeV.

9.4.9 Discussion of task force conclusions

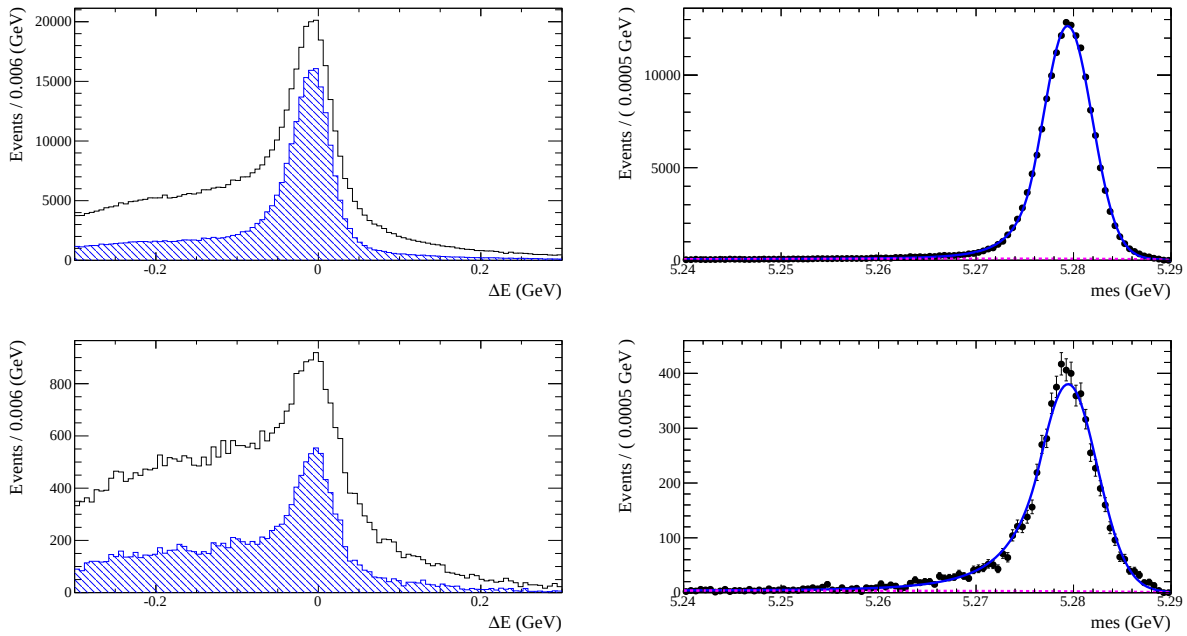

Figure 9.50: ΔE (left) and $m_{\rm ES}$ (right) of $B^- \to D^0\pi^-$ with $D^0 \to K^-\pi^+\pi^0$ reconstruction. Two histograms in each ΔE plot are before and after D^0 mass cut. Top: both γ's are in barrel and forward endcap; bottom: one γ in the backward.

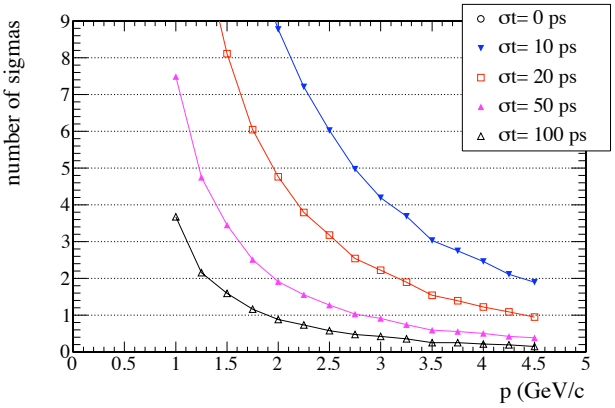

Figure 9.53: Kaon-pion separation versus measured momentum for different time resolutions in the backward EMC region. The finite separation for perfect timing resolution is because measured momentum is used.

Bibliography

[1] W. -S. Hou, "Enhanced charged Higgs boson effects in $B^- \to \tau\bar{\nu}$, $\mu\bar{\nu}$ and $b \to \tau\bar{\nu} + X$," Phys. Rev. D **48** (1993) 2342-2344.

[2] W. Altmannshofer, A. J. Buras, D. M. Straub, M. Wick, "New strategies for New Physics search in $B \to K^*\nu\bar{\nu}$, $B \to K\nu\bar{\nu}$ and $B \to X_s\nu\bar{\nu}$ decays," JHEP **0904**, 022 (2009).

[3] P. del Amo Sanchez *et al.* [BABAR Collaboration] "Search for the Rare Decay $B \to K\nu\bar{\nu}$," Phys. Rev. D **82**, 112002 (2010).

[4] P. del Amo Sanchez *et al.* [BABAR Collaboration], "Search for the Rare Decay $B \to K\nu\bar{n}u$," Phys. Rev. D **82**, 112002 (2010).

9.5 Trigger

This is a reminder that we need a synopsis of the EMC trigger somewhere in the EMC chapter, although the detailed description will be in the ETD chapter. It is to be determined whether this should be in a separate section or merged with the three sub-calorimeter sections.

9.5.1 Calorimeter readout trigger

9.5.1.1 Normal mode

9.5.1.2 Calibration mode

9.5.2 Calorimeter trigger primitives

9.6 Detector protection

Personnel ES&H will be elsewhere.

9.6.1 Thermal shock

9.6.2 Mechanical shock, including earthquakes

9.6.3 Fluid spills

9.6.4 Electrical surges, outages

9.6.5 Radiation damage

Radiation exposure from Bhabha, Touschek and beam-gas scattering is monitored by a set of 56 realtime integrating dosimeters (Rad-FETs) placed in front of the barrel and 60 RadFETs in front of the endcap. The accumulated dose, measured by these RadFETs over the life of the *BABAR* detector, along with the observed loss in scintillation light output is shown in Figure[**?**], separately for the endcap, the forward, and the backward barrel of the calorimeter. The dose over the life of Super$B$ is expected to be two orders of magnitude greater.

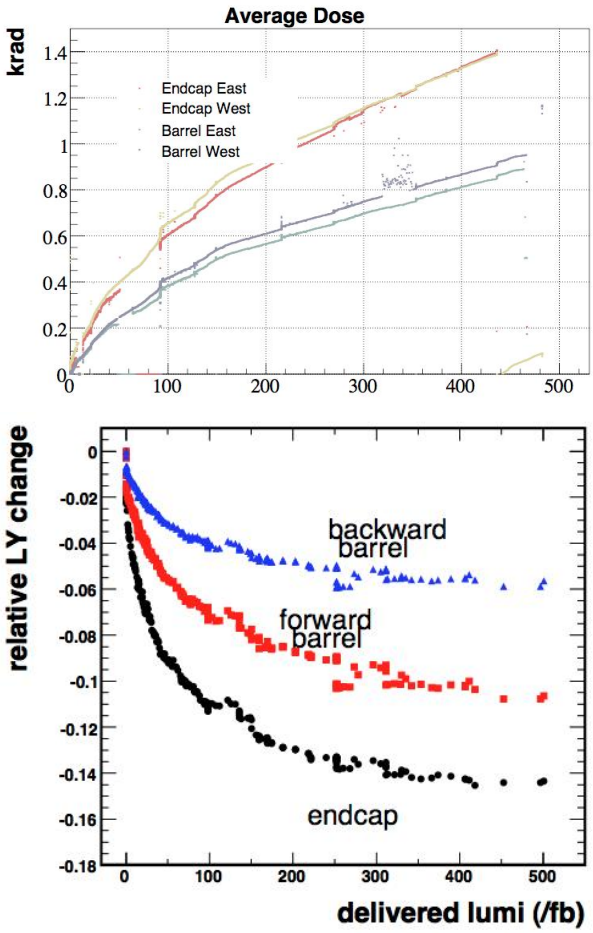

Figure 9.54: Left: Radiation dose as measured by RadFETs in the *BABAR* barrel and endcap. Right: Decrease in light output with radiation dose for the *BABAR* CsI(Tl) barrel and endcap.
These figures are placeholders; we need higher quality copies.

9.7 Cost & Schedule

This will appear elsewhere.

9.7.1 WBS structure

9.7.2 Gantt chart

9.7.3 Basis of estimates

9.7.4 Cost and schedule risks

Bibliography

[1] The EMC bibliography items should be placed in the file `EMC/EMC-bibliography.tex`.